

The influence of crustal magnetic fields on the Martian bow shock location: a statistical analysis of MAVEN and Mars Express observations

P. Garnier¹, C. Jacquy¹, X. Gendre², V. Génot¹, C. Mazelle¹, X. Fang³, J.R. Gruesbeck^{4,5}, B. Sánchez-Cano⁶, J.S. Halekas⁷

¹IRAP, Université de Toulouse, CNES, CNRS, UPS, (Toulouse), France

²ISAE-SUPAERO, Université de Toulouse, 10 Avenue Edouard Belin, 31055 Toulouse, France

³Laboratory for Atmospheric and Space Physics University of Colorado, Boulder, US

⁴Department of Astronomy, University of Maryland, College Park, MD, US

⁵NASA Goddard Space Flight Center, Greenbelt, MD, US

⁶School of Physics and Astronomy, University of Leicester, Leicester, UK

⁷Department of Physics and Astronomy, University of Iowa, Iowa City, Iowa, USA.

Key Points:

- The influence of crustal magnetic fields on the Martian shock is significant based on the first multi-mission study
- The strongest crustal field region has a major influence in a large angular range, when close to noon and when the IMF is stable.
- The crustal field influence varies with season, showing a coupling between crustal fields, the ionosphere and the shock

Corresponding author: Philippe Garnier, philippe.garnier@irap.omp.eu

This article has been accepted for publication and undergone full peer review but has not been through the copyediting, typesetting, pagination and proofreading process, which may lead to differences between this version and the [Version of Record](#). Please cite this article as [doi: 10.1029/2021JA030146](https://doi.org/10.1029/2021JA030146).

This article is protected by copyright. All rights reserved.

Abstract

Previous missions underlined the complex influence of the crustal magnetic fields on the Martian environment, including the plasma boundaries. Their influence on the bow shock is however poorly constrained, with most studies showing North/South differences attributed to the crustal fields, with various conclusions from little to strong variabilities.

We analyze for the first time in detail the influence of crustal fields on the Martian shock location based on a multi-mission analysis (MAVEN and MEX). We introduce the angular distance to the strongest crustal field region in the southern hemisphere that induces the largest influence (but not unique, with a minimum pressure threshold analyzed). Its impact is at large scale ($> 40 - 60^\circ$ around), is modulated by the local time of the strongest source region (with no influence beyond terminator), and maximizes when the Interplanetary Magnetic field (IMF) is stable during the preceding hours. We introduce a technique, i.e. partial correlations, to provide a coherent picture for both MAVEN/MEX due to existing cross correlations with Extreme UltraViolet (EUV).

A composite parameter is proposed, that represents the combined influence of EUV, magnetosonic mach number (two major drivers) and crustal fields, the latter having an impact of hundreds of km. The influence of crustal fields on the shock appears seasonal and correlated with the Total Electronic Content, revealing a large scale coupling between the crustal fields, the ionosphere and the shock. The crustal field influence on the shock is thus significant and complex, with a coupling to both the ionosphere below and the IMF above.

1 Introduction

The Martian interaction with the solar wind (SW) is unique due to the absence of a global intrinsic dynamo magnetic field but with the presence of remnant crustal magnetic fields (Acuña et al. (2001)). The Mars Global Surveyor (MGS; 1997-2006), Mars Express (MEX; 2004-present) and Mars Atmosphere and Volatile Evolution (MAVEN; 2014-present) missions have revealed major effects of the crustal fields on the Martian induced magnetosphere through various phenomena, such as: plasma precipitation (Brain et al. (2007), Fang et al. (2010), Lillis and Brain (2013)) and induced auroras (Bertaux et al. (2005), Schneider et al. (2018)), density depletions (Mitchell et al. (2001), Hall et

51 al. (2016a), Steckiewicz et al. (2017), Flynn et al. (2017)), ion escape (Fang et al. (2010),
52 Ma et al. (2014), Romanelli et al. (2018), Poppe et al. (2021)), cross terminator trans-
53 port (Xu et al. (2016), Fang et al. (2015)), and magnetic reconnection in the tail region
54 (DiBraccio et al. (2018)).

55 The interaction between Mars and the solar wind results in several plasma bound-
56 aries, such as the bow shock (hereafter BS), the Induced Magnetospheric Boundary (IMB)
57 or Magnetic Pile-Up Boundary (MPB), the Ion Composition Boundary (ICB), the Pho-
58 toElectron Boundary (PEB) or the ionopause. These boundaries are highly dynamic and
59 depend on both internal and external drivers. Studying their dynamics is crucial to bet-
60 ter understand the response of the Martian environment and thus its evolution with time.
61 The SW dynamic pressure was considered as a major driver for the BS and MPB loca-
62 tion (Vignes et al. (2002), Crider (2004)). Edberg et al. (2010) showed that the magne-
63 tosonic mach number of the SW also influences significantly the BS. Later, Hall et al.
64 (2016b) analyzed MEX data and showed that the BS location is more sensitive to sea-
65 sonal variations in the solar extreme ultraviolet (EUV) irradiance than to SW dynamic
66 pressure variations, and Hall et al. (2019) also showed the influence of solar cycle EUV
67 variations. Moreover, Halekas et al. (2017) showed the major influence of the magnetosonic
68 mach number and EUV, as well as a significant influence of SW dynamic pressure but
69 a weak dependance on the geographical longitudes (which would have been expected due
70 to non-uniformly distributed crustal fields).

71 Among the various drivers of the BS location, the crustal magnetic fields of the planet
72 are among the least understood. Previous studies suggested an influence of the crustal
73 fields, characterized by differences between the north and south locations of BS (e.g. Mazelle
74 et al. (2004)), presumably attributed to the strongest crustal source region located in
75 the southern hemisphere of the planet (centered on $\sim -45^\circ$ IAU latitude and $\sim 180^\circ$
76 IAU longitude). Such hemispheric differences were also observed for other boundaries
77 (Matsunaga et al. (2017), Garnier et al. (2017)). However, these comparisons showed a
78 weak dependance on the position of the strongest crustal source region, with no clear lon-
79 gitude modulation found. Edberg et al. (2008) proposed wide (i.e. 120°) longitude bins
80 exhibiting large differences in terms of BS location, these differences being found much
81 smaller with MAVEN by Halekas et al. (2017). Gruesbeck et al. (2018) showed that the
82 strongest crustal source region in the southern hemisphere had a different influence on
83 the BS location depending on the dayside vs nightside location of the source region. Fang

84 et al. (2017) (hereafter XF17) also suggested a rather global influence of the crustal field
85 on the BS, and that the crustal magnetic pressures over different solar zenith angle zones
86 exert different influences. Recently, Nemec et al. (2020) compared the influence of EUV,
87 SW dynamic pressure and local crustal field intensity on the MAVEN BS crossings, sug-
88 gesting a non negligible influence of local crustal fields but still much smaller compared
89 to the other two drivers. Overall, the influence of the crustal fields on the BS is still un-
90 der debate - from little influence (Edberg et al. (2009), Li et al. (2020)) to strong vari-
91 ability, up to above 1000 km altitude differences in the BS location based on North/South
92 asymmetries (Edberg et al. (2008), Gruesbeck et al. (2018)) - or in terms of local (Nemec
93 et al. (2020)) vs more global (Fang et al. (2017)) spatial extent. For these reasons, the
94 main goal of this study is to do the best-to-date characterization of the behaviour of the
95 Martian BS over crustal fields using all available datasets.

96 In this paper we analyze shock crossing datasets from both the MEX and MAVEN
97 missions. We describe the data in Section 2.1 and our methods in Section 2.2. The re-
98 sults of our study are shown in Section 3, starting with a detailed analysis of the influ-
99 ence of the crustal fields on the Martian shock location in Section 3.1. Then in Section
100 3.2 we use a partial correlation approach to investigate existing biases vs Extreme UL-
101 traViolet fluxes and confirm the significance of the crustal field influence on the shock
102 location. We finally provide a discussion and conclude in Sections 4 and 5.

103 **2 Datasets and methods**

104 **2.1 Description of the datasets**

105 We analyze the observations by two missions - MEX and MAVEN - to support the
106 results obtained and avoid biases related to mission specificities.

107 We first used the list of MEX crossings derived by Hall et al. (2016b), in which an
108 automatic algorithm is used to detect the BS crossings in the measurements from the
109 MEX instrument Analyzer of Space Plasmas and Energetic Atoms (ASPERA-3) Elec-
110 tron Spectrometer (ELS). The ASPERA-3 ELS is an electron spectrometer able to de-
111 tect electrons in the energy range of 1 eV-20 keV with an energy resolution of around
112 8% (Barabash et al. (2006)). From January 2004 to May 2015, 12091 BS crossings were
113 identified. Among these, we reduced multiple crossings occurring within a minute into
114 one event, leading to 11,820 crossings in total for the MEX BS.

115 Two MAVEN studies dealing specifically with the analysis of the BS boundary -
116 XF17 (who used the list published by Masunaga et al. (2017)) and Gruesbeck et al. (2018)
117 - provided lists of 2934 and 1957 BS crossings over the periods november 2014 to march
118 2016 and november 2014 to march 2017 respectively. These crossings were identified based
119 on the MAVEN MAG magnetic field data (Connerney et al. (2015)), SWEA electron data
120 (Mitchell et al. (2016)), and SWIA ion data (Halekas et al. (2015)). We removed the cross-
121 ings that overlapped in time or occurred at the same time within an hour, reducing our
122 MAVEN list to 3837 BS crossings.

123 The large number of BS crossings of MEX and MAVEN - thanks to their relatively
124 short orbital periods of 6.7 and 4.5 hours respectively - provides a large spatial and tem-
125 poral coverage for statistical analyses. The coverage in terms of solar EUV flux and SW
126 dynamic pressure, known as significant drivers, is also sufficiently broad (see the dataset
127 descriptions by Hall et al. (2016b) and Masunaga et al. (2017)). However, a notewor-
128 thy difference exists between both datasets: MEX covers a whole solar cycle (2004-2015,
129 with the solar maximum in 2014), while the MAVEN dataset corresponds to a shorter
130 period (2014-2017) where the mean EUV level (given by the solar 10.7 *cm* radio flux)
131 was larger by $\sim 14\%$ at the time of the crossings compared with the MEX dataset. Since
132 the absolute location of the BS may be different between both datasets due to solar ac-
133 tivity variability (see Section 3.1), we thus focus on the variability of the BS location rather
134 than on their absolute values.

135 Moreover, we use a third dataset based on the Mars Global Surveyor (MGS) mis-
136 sion data analysis by Vignes et al. (2002). MGS included a dual fluxgate magnetome-
137 ter (MAG) and an electron reflectometer (ER) (Acuña et al. (1992)). This third dataset
138 contains 544 BS crossings occurring during the pre-mapping phase of the mission where
139 the orbit was eccentric enough to cross the shock. However, this third dataset is consid-
140 ered with caution, since the number of crossings is limited compared to the MEX and
141 MAVEN datasets. Furthermore, the dataset crossings occurred over a single year (from
142 September 1997 to September 1998, after the solar minimum in 1996) when a relatively
143 narrow range of EUV fluxes (3 times smaller than MAVEN) and solar wind properties
144 were covered.

145 Finally, we use in Section 4 Total Electronic Content ionospheric data from the MAR-
146 SIS instrument onboard MEX. TEC retrievals are given from the planetary surface un-

147 til MEX altitude, and are obtained when MARSIS operates in the subsurface mode (see
 148 more at Sánchez-Cano et al. (2015)). The algorithm for the retrieval is described in Cartacci
 149 et al. (2013) and Cartacci et al. (2018). Only data with a signal to noise ratio > 15 dB
 150 were used to remove noise and bad quality data.

151 2.2 Description of the methods

152 2.2.1 The extrapolated terminator altitude of the shock

153 We use a one-dimensionnal approach to investigate the variability of the BS loca-
 154 tion, by considering the so-called extrapolated terminator altitude, defined as follows.

We first rotate (by 4°) the crossing locations into the SW aberrated cylindrical MSO system, to account for the aberration of the solar wind flow direction by the planetary orbital motion. The MSO frame (X,Y,Z) coordinates are defined as follows: X points towards the Sun, Y points approximately opposite to Mars orbital angular velocity and Z completes the right-handed set. We neglect the axis asymmetry of the BS (see Fang et al. (2015)) and assume the shock boundary can be fitted by a conic section described by the following equation:

$$r = \frac{L}{1 + e \cos(\theta)} \quad (1)$$

where r is the distance to the focus located at $(X_0, 0, 0)$, L and e are respectively the semi-latus rectum and eccentricity. As performed by previous authors (see e.g. Edberg et al. (2008) or Hall et al. (2016b)), we calculate the extrapolated terminator altitude, defined by the altitude of the conic in the aberrated terminator plane:

$$R_{TD} = \sqrt{L^2 + (e^2 - 1) \cdot X_0^2 + 2 \cdot e \cdot L \cdot X_0} - R_M \quad (2)$$

155 where R_M is the Martian radius (3390 km). This parameter represents the variability
 156 of the BS location, removing the strong solar zenith angle influence by projecting the
 157 crossing point toward the aberrated terminator along an assumed conic fit. This sim-
 158 ple procedure prevents from doing complex analysis of 3D asymmetries as done by Gruesbeck
 159 et al. (2018), but is efficient to focus on a single parameter influence (e.g. the crustal fields).
 160 We used the L and e values published by Hall et al. (2016b) for the MEX crossings ($L =$
 161 $1.82 R_M$, $e = 1.01$), and the values published by XF17 for MAVEN ($L = 2.303 R_M$,
 162 $e = 0.872$). Note the impact of using various data sets and conic fit parameters is dis-
 163 cussed further in Section 3.2.

164 Note that we could wonder whether a one-dimensionnal approach, that projects
165 the crossing point along a conic fit, is appropriate to investigate local variabilities of the
166 shock location such as induced by crustal fields. However, first the magnetosonic waves
167 do not propagate radially only, the impact of crustal fields after magnetosonic wave prop-
168 agation upstream of the planet will thus necessarily influence the shock location in a rather
169 wide region given the distance of the shock. Second, if the influence was very localized
170 at the shock location, this would have been observed earlier, and is in contradiction with
171 the large extent of the influence shown in the following sections, which confirms the abil-
172 ity of the one-dimensionnal approach to study the crustal field influence.

173 *2.2.2 Statistical tools*

174 Beyond the direct analysis of the extrapolated terminator altitude, we use in this
175 paper correlation approaches defined below: linear Pearson correlation coefficients, un-
176 paired t-tests and partial correlations.

177 First, simple correlation factors are analyzed in Sections 3.1 and 3.2. By default,
178 we consider in the paper Pearson correlation coefficients that inform us about the strength
179 and direction of the linear relationship between two variables, with values ranging from
180 -1 (perfect anti-correlation) to $+1$ (perfect correlation).

181 In order to evaluate the significance of the correlation factor which strongly depends
182 on the sample size, we make statistical tests. A t-test evaluates the test statistics asso-
183 ciated with the correlation, and compares it with a threshold defined for a given risk.
184 This threshold corresponds to the statistics of the null hypothesis H_0 , which is the hy-
185 pothesis of no significant correlation. The correlation is considered significant if the test
186 statistics t is above the threshold, otherwise the correlation factor is not considered sig-
187 nificant with sufficient confidence. The risk value chosen by default for calculating the
188 threshold is 5%, corresponding to a 2 standard deviations (i.e. 95%) tolerance interval
189 for a gaussian probability distribution. Alternatively, two-sided p-values can be calcu-
190 lated to provide the probability that the null hypothesis is true. If the p-value is larger
191 than the risk limit assumed (5% here), there is insufficient confidence that a significant
192 linear relationship exists. On the other hand, if the p-value is smaller than the limit risk
193 considered, the null hypothesis is rejected and the correlation is considered significant.

194 In the rest of the paper we will mention that p-values are negligible when they are smaller
195 than 10^{-5} and note them with "(n)".

196 Unpaired t-tests are also used in Section 3.2. These procedures compare two in-
197 dependent groups to determine if there is a significant difference between them. They
198 assess whether the two groups have significantly different mean values. P-values can also
199 be associated to these tests as for correlation tests.

200 Beyond these well known methods - linear Pearson correlation coefficients and un-
201 paired t-tests -, we use a partial correlation approach in Section 3.2 to mitigate possi-
202 ble biases due to cross correlations between drivers. The partial correlation approach (Baba
203 et al. (2004); see Appendix A for a detailed description of the method) identifies indi-
204 vidual relationships among variables that may be correlated, and calculates the corre-
205 lation coefficients - and estimates their significance - between two variables after control-
206 ling for the influence of other variables. This technique is not a common tool in the lit-
207 erature, but it has been successfully used by several authors in studies such as the so-
208 lar wind Earth interaction (Kim et al. (2011), Simms et al. (2021)), solar physics (Trottet
209 et al. (2015), Le and Zhang (2017)), surface planetology (Anderson and Bell (2013)) and
210 galaxies and compact objects (Dai et al. (2018), Kang et al. (2018), Yesuf and Ho (2019),
211 Ni et al. (2020)).

212 For example, if one considers only three variables that are possibly correlated (x ,
213 y , z), the partial correlation between x and y , after controlling for z , is calculated as fol-
214 lows: first the linear regression between x and z is performed, and the residuals are given
215 by the difference between the x values and the regression. Subtracting the regression line
216 removes the linear influence of z on x . Residuals are then calculated for y with the same
217 procedure to remove the linear influence of z on y . The partial correlation coefficient be-
218 tween x and y , after controlling for the third variable z , is simply determined by the Pear-
219 son correlation coefficient between these two residuals. This technique can be general-
220 ized to a larger number of variables.

221 The relations are assumed linear with this technique ($y = a + \sum_i x_i \cdot b_i$ with a in-
222 tercept and b_i slopes), but can also correspond to power law relations (of the type $y =$
223 $a \prod_i x_i^{b_i}$) when linearized with a logarithm. As for direct correlations, the linear assump-
224 tion is actually a weak assumption and does not need linear relationships between the
225 parameters to remain valid, since the linear assumption keeps true at first order in most

226 cases. In order to evaluate the significance of the partial correlation factors, as for zero-
227 order correlations, a t-test can be performed to evaluate the test statistics that shall be
228 larger than the threshold associated to the null hypothesis H_0 , and p-values provide the
229 probability that the null hypothesis is true (i.e. that there is no significant partial cor-
230 relation).

231 In the rest of the paper, correlations factors and significance test statistics and p-
232 values by default correspond to direct linear correlations, the use of the partial corre-
233 lations is explicitly specified.

234 3 Results

235 3.1 The influence of crustal fields: local vs global influence

236 Several authors attempted to analyze the influence of the crustal fields on the BS
237 location. The first obvious way is to consider correlations with the geographical longi-
238 tude, to uncover the influence of the strongest crustal source region located in the south-
239 ern hemisphere at $\sim [150\ 230]^\circ$ East longitude and in the $\sim [-90\ 0]^\circ$ latitude range (see
240 the crustal field map in Figure 3d). Edberg et al. (2008) used this approach for MEX
241 but could only obtain a rough trimodal behavior with three wide (i.e. 120°) longitude
242 bands with different BS distances attributed to the crustal sources influence. Neverthe-
243 less, as cautioned by XF17, the longitudinal position provides only partial but not full
244 information of the orientation of the strongest crustal field region with respect to the im-
245 pinging solar wind, the latter of which is critical for determining the bow shock forma-
246 tion and location. Overall, most authors essentially attributed the presence of a hemi-
247 spheric asymmetry to crustal fields (Mazelle et al. (2004); Gruesbeck et al. (2018)). On
248 the other side, Nemec et al. (2020) recently quantified the dependence of the stand-off
249 distance of the Martian BS with respect to local crustal fields, using the local crustal field
250 at 400 km altitude from the Morschhauser et al. (2014) model, to show their influence
251 is non negligible but much smaller than EUV or SW dynamic pressure.

252 We also performed a direct longitude dependence analysis using the MEX and MAVEN
253 datasets (not shown here), showing no clear dependence except by selecting large lon-
254 gitude bands as performed by Edberg et al. (2008). However, one can refine the anal-
255 ysis by considering only a $(\pm 20^\circ)$ latitude band around the strongest crustal source re-
256 gion located around $\sim -45^\circ$ latitude and $\sim 180^\circ$ longitude. This leads to focus on a

257 latitude band with a highly variable crustal field intensity around the planet (see Fig-
 258 ure 3d where the latitude band limits are superimposed on the crustal field map). The
 259 result is shown in Figure 1 for the three datasets (MAVEN, MEX and MGS). A pattern
 260 with a "smile" shape is suggested and is roughly consistent among the three missions,
 261 with a minimum BS terminator altitude R_{TD} at small/large longitudes (corresponding
 262 to weak crustal field regions, see the colorbar) and a maximum value near $\sim 180^\circ$ East
 263 longitude where the strongest crustal source region is located. The MEX median pro-
 264 file (and the percentiles area) shows a clear modulation with a minimum in the range
 265 270° to 20° (the two strongest minima of crustal fields being located close to $270-280^\circ$
 266 and around $360/0^\circ$). The MAVEN median curve is more flat except a clear peak at $180-$
 267 225° and a low point at $360/0^\circ$, but the small dips of MAVEN seem close to crustal field
 268 intensity gaps. The MGS median curve is noisy, but overall also consistent with a "smile"
 269 shape.

270 Moreover, taking the terminator altitude vs the cosine of the longitude (translated
 271 into the range -180° to 180°) leads to correlation coefficients of -0.10 and -0.11 for MAVEN
 272 and MEX. The correlation is negative since the strongest crustal source region is cen-
 273 tered on $\cos(longitude) = -1$ while larger cosine values correspond to regions farther
 274 from the strongest crustal source region. These correlations may seem small but are still
 275 statistically significant given the large number of points, with p-values of about $4 \cdot 10^{-3}/2 \cdot$
 276 10^{-8} respectively for MAVEN/MEX, i.e far below the 5% commonly considered as an
 277 acceptable value. In absolute values, the average BS altitude decreases by 300 km (290/310
 278 km for MAVEN/MEX) from the longitude sector ($135-225^\circ$ East longitude) of the strongest
 279 crustal source region to sectors away from it.

280 The correlation for the MGS dataset is also negative (~ -0.12 , with a p-value of
 281 0.04) but is closer to the significance limit due to the lower number of data. Due to the
 282 relatively low number of events and smaller significance, we mostly focus on the MEX
 283 and MAVEN datasets in the rest of the paper, and only briefly mention the MGS data
 284 analysis to discuss the consistence among the mission observations.

285 We further investigate whether the crustal field influence is global or local. We cal-
 286 culated the correlation between the terminator altitude and either the angular averaged
 287 pressure of the crustal magnetic field $B^2/(2\mu_0)$ or the angular averaged crustal magnetic
 288 field magnitude. B is the crustal magnetic field magnitude at 400 km altitude from Morschhauser

289 et al. (2014) averaged over an area defined by a variable angular range around the sub-
290 spacecraft location of the spacecraft: e.g. 40° range means we average the crustal field
291 pressure or the crustal field intensity over an angular range (based on spherical distance
292 calculations) of 40° around the exact longitude/latitude of the crossing, while 0° means
293 we consider the pressure at the exact longitude/latitude of the crossing (i.e. the local
294 value with no averaging). Such analysis, shown in Figure 2, reveals a positive correla-
295 tion for both MAVEN/MEX increasing until a maximum for $70 - 80^\circ$ angular range.
296 The correlation for MAVEN/MEX with the crustal pressure rises from 0.04/0.11 at 0°
297 to 0.18/0.33 at $70-80^\circ$ angular range (with statistical significant correlations even for
298 0° angular range and negligible p-value at maximum correlation). Similar peak corre-
299 lations (even slightly larger for MAVEN) are observed when considering the crustal field
300 intensity instead of the pressure, but the profile becomes more flat with a less pronounced
301 peak. Note that using an even smaller power law index for the crustal field intensity, such
302 as $(B^2/(2\mu_0))^{1/6}$ as used by XF17, also leads to similar results with close peak correla-
303 tion factor values and an even more flat profile (more and more flat when smaller power
304 law index values of the pressure are considered). The correlation between the termina-
305 tor altitude of the BS and the crustal fields (either the pressure, or powers law values
306 of it) is always significant, but maximizes for a large angular range considered. Our re-
307 sults suggest a rather global influence (slightly less than hemispheric) of the crustal field
308 pressure on the BS location, in closer agreement with the finding by XF17 rather than
309 the approach considered by Nemec et al. (2020).

310 We also convolved the crustal field pressure with an angular Gaussian filter (with
311 a variable standard deviation σ defined dynamically) to evaluate the influence of the crustal
312 fields at the sub-spacecraft location compared to farther longitudes/latitudes, leading
313 to similar maximum correlation values for $\sigma > 60^\circ$ (not shown). The need for large an-
314 gular ranges is expected based on the large distance of the BS boundary, and is in agree-
315 ment with previous studies showing a rather global influence. Note that the MGS BS
316 dataset also suggests an increasing correlation between the BS distance and the angu-
317 lar range (with a peak at 110° and a maximum correlation factor of 0.4). Any functional
318 forms of the BS location variability with respect to the crustal fields thus need to con-
319 sider the large-scale effect of the crustal fields rather than a local effect: the small power
320 law index value (0.018) associated with the local crustal field pressure influence on the

321 Martian BS location by Nemeč et al. (2020) thus inevitably underestimated the crustal
322 field effects due to the limitation of using only local crustal field distributions.

323 Figure 3 provides another examination of the local vs global influence of the crustal
324 fields on the BS location. It shows the logarithmic value of the occurrence frequency of
325 the MAVEN/MEX BS crossings as a function of the terminator altitude and of the an-
326 gular distance from the strongest crustal source region (assumed at $\sim -45^\circ$ latitude and
327 $\sim 180^\circ$ East longitude, see Figure 3d)). The angular distance is the angle between the
328 planetary center - spacecraft vector and the planetary center - strongest crustal source
329 region center vector. The occurrence frequency is simply the number of shock crossings
330 counted in each cell of the 2 dimensional grid defined by the angular distance and the
331 terminator altitude, then given in % of the total number of crossings. We use the an-
332 gular distance to consider that the crustal field may influence the plasma environment
333 and thus the BS boundary in any direction, not only along the longitude.

334 Both MAVEN/MEX results (Figures 3a and 3b) are very similar and reveal a dom-
335 inant influence of the strongest crustal field region, with the BS altitude decreasing far-
336 ther from it. The errorbars of the distribution are large probably due to the presence
337 of all other parameters of influence (SW pressure, solar EUV...). The mean altitude is
338 larger in the $0 - 80/90^\circ$ angular distance range than beyond, which is consistent with
339 the maximum correlation for $70 - 80^\circ$ angular range as seen in Figure 2. However, a plateau
340 appears in both datasets in a narrower angular range $0 - 40/60^\circ$ that is consistent with
341 a dominant influence of the strongest crustal field region whose angular extent is of the
342 same order of magnitude (see Figure 3d). On top of the major trend, we notice a slight
343 lift in the BS altitude in the $\sim 110 - 140^\circ$ angular distance range, which could be at-
344 tributed to the strong secondary crustal field sources located at such angular distances
345 near the equator (see same panel). The trend in the MAVEN dataset is more prominent
346 than in the MEX dataset, which will be discussed later. Moreover, despite a poorer cov-
347 erage, the MGS dataset also shows the decrease of the BS distance with angular distance.

348 One of the challenges of disentangling the crustal field influence is the presence of
349 many other driving factors, including the dynamics of the incident SW and IMF. Indeed,
350 the crustal fields act as pressure enhancements, induce currents that propagate into the
351 Martian plasma environment, through a complex interplay between the incident mag-
352 netosheath plasma transport and the magnetic field topology arising from the draping

353 of the Interplanetary Magnetic Field (IMF) around the planet and modified by the plan-
 354 etary crustal fields themselves. The whole interaction is driven by the SW plasma and
 355 magnetic field, whose orientation varies with time. When the IMF rotates at short timescales,
 356 the influence of the crustal fields, that is essentially a geographical influence in the plan-
 357 etary frame with a larger timescale, may be partially masked due to the rotation of the
 358 interaction. Several external or internal drivers control the BS location, but the IMF ro-
 359 tation may partially hide the geographical influences such as crustal fields.

360 Figure 3c shows the same MAVEN map as Figure 3a, but we superimposed mean
 361 values during the periods of low and high IMF clock angle variabilities. The IMF clock
 362 angle was calculated from the upstream conditions prior to the BS crossings, defined as
 363 $\tan^{-1}(B_{Z_{IMF}}/B_{Y_{IMF}})$. We use the standard deviation of the clock angle over the two hours
 364 before the crossings as a measure of the rotation dynamics of the IMF, and divide the
 365 whole MAVEN dataset into one low (i.e. below the median standard deviation value)
 366 and one high (i.e. above the median standard deviation value) variability dataset. Panel
 367 c shows the mean R_{TD} of the BS for both sub-samples. As expected, the crustal field
 368 influence is less visible under high IMF clock angle variability conditions than under the
 369 low variability conditions, where the altitude difference is as high as up to 1000 km.

370 The dynamics of the IMF can actually impact the BS at several levels that should
 371 be further analyzed in the future. In particular, a constant IMF or a sudden change of
 372 IMF to the same strength and orientation may have different effects on the BS locations.
 373 Depending on the conditions considered, the BS shape can be modified, with asymme-
 374 tries of the global shape appearing, or a sudden compression followed by a recovery phase
 375 depending on the mach number and on the dynamic pressure. Previous studies at Earth
 376 or Venus also suggested that a rotation of the IMF could have different consequences wether
 377 the local conditions lead to perpendicular or parallel shocks with higher perpendicular
 378 BS locations in particular in the tail (Wang et al. (2016)). At Venus or Mars authors sug-
 379 gested asymmetries of the BS location depending on the orientation of the $\vec{E} = -\vec{V} \times \vec{B}$
 380 electric field that increases the mass loading due to accelerated pickup ions (Alexander
 381 et al. (1986), Vignes et al. (2002)).

382 We performed another correlation analysis between the BS terminator altitude and
 383 the crustal fields, by including a maximum threshold on the crustal field intensities (lo-
 384 cal values at 400 km altitude) considered in the analysis. The results show that no sig-

385 nificant correlation between local crustal field intensities and the BS location appears
386 as long as only intensities below a few nT are considered. The correlation then rises when
387 the threshold increases to include stronger and stronger sources. This shows that, even
388 when considering only local crustal fields instead of angular averaged values, a large num-
389 ber of regions around the planet (intensities of few nT are observed in a many regions)
390 can influence the BS location beyond the southern hemisphere strongest crustal source
391 region. Nonetheless, the large size and strong intensity of the crustal fields in this region
392 make it the major crustal field region driver.

393 Gruesbeck et al. (2018) also showed a significant influence of the local time of the
394 strongest crustal source region on the 3D shape of the BS when it was located on the
395 dayside vs on the nightside. Figure 4 shows how the location of the strongest crustal source
396 region impacts the BS distance using both MAVEN and MEX datasets. Despite large
397 data scattering - with a standard deviation of ~ 1000 km - due to the combined effects
398 of other driving factors, the average BS R_{TD} altitude is modulated by the MSO longi-
399 tude (hereafter ϕ_{mso} , equivalent to local time) of the strongest crustal field region: the
400 BS standoff distance peaks when the strongest crustal field region is located at noon. A
401 similar trend may also be seen with the MGS dataset with clear peak at noon longitude.
402 The mean profile suggests a reduced and steady or inexistent influence of the strongest
403 crustal source region when it is located on the nightside.

404 These results thus suggest a dominant (but not unique) influence of the strongest
405 crustal field region (with a large angular extent consistent with its size) on the BS lo-
406 cation. This influence depends on the stability of the IMF orientation that may partially
407 hide the crustal field influence, as well as on the local time of the strongest crustal source
408 region. Regarding the latter, the information corresponding to the increased crustal field
409 pressure by the strongest crustal source region rotation propagate upward at the fast mag-
410 netosonic wave velocity, and then probably impact the location of the BS. The informa-
411 tion reaches the solar wind flow faster at noon on the dayside than on the nightside due
412 not only to the closer distance, but also to the fact that the magnetosonic waves from
413 the nightside are partially attenuated, and the dayside fast mode magnetosonic wave speed
414 is expected to be larger due to the increased magnetic field in the draping region. Con-
415 sequently, enhanced crustal fields impact the BS surface, which is significantly reduced
416 when the strongest crustal source region is located far from the noon direction. Figures
417 3 and 4 show that the crustal field can enhance the extrapolated terminator altitude of

418 the Martian BS by several hundreds of km on average. This is in agreement with the large
419 possible range mentioned in the literature, ranging from no or little influence (with e.g.
420 about 100 km influence from MEX observations (Edberg et al. (2009)) or simple dipole
421 based MHD simulations (Li et al. (2020))) to ~ 400 km altitude fluctuation according
422 to XF17, and even above 1000 km influence based on North vs South asymmetries (Edberg
423 et al. (2008), Gruesbeck et al. (2018)).

424 3.2 Investigating statistical biases

425 The previous section shows strong evidences regarding the influence of the crustal
426 fields on the distance of the Martian BS, through several spacecraft and several meth-
427 ods providing consistent results: geographical longitude modulation, correlation vs crustal
428 field pressure with a variable angular range, direct plotting of the distance vs the angu-
429 lar distance from the strongest crustal source region, location of the strongest crustal source
430 region with respect to noon. However, differences arise between MAVEN and MEX, with
431 higher absolute BS distances and an apparently stronger influence of the angular distance
432 from the strongest crustal field region for MAVEN than for MEX.

433 The MAVEN and MEX datasets used in this study cover different periods (respec-
434 tively 2014-2017 and 2004-2015), corresponding to different EUV conditions. The large
435 MEX dataset provides a wide range of EUV conditions, with a full solar cycle (includ-
436 ing the lower and extended ever recorded solar minimum), while the MAVEN dataset
437 corresponds to a period with an active Sun in 2014 and 2015 (where most of our MAVEN
438 crossings occurred) below a declining activity in 2016-2017. The mean EUV level of the
439 MAVEN crossings (given by the solar 10.7 *cm* radio flux) was thus larger by $\sim 14\%$ com-
440 pared with the MEX dataset. The larger EUV conditions associated to the MAVEN dataset
441 certainly contribute to the larger BS distances observed (by $\sim 5\%$) for MAVEN than
442 for MEX. The EUV fluxes increase indeed the ionospheric scale height and the ioniza-
443 tion rate of the Martian atmosphere, which adds mass to the solar wind flow through
444 pickup ions and slows down the solar wind, then creating a larger apparent obstacle that
445 pushes the BS further. The compared magnetosonic mach number conditions, which also
446 have a major influence on the BS location through the Mach cone conditions, may also
447 have induced this absolute difference in the BS altitude between both missions, however
448 these conditions are not known precisely for the pre-MAVEN period.

449 A dedicated analysis also reveals a significant bias on the MAVEN dataset due to
 450 the EUV conditions during the BS crossings. Figure 5 provides the EUV values and oc-
 451 currence frequency vs either the angular distance from the strongest crustal source re-
 452 gion center or its MSO longitude for both missions. The EUV values were determined
 453 for MAVEN from the FISM model (Chamberlin et al. (2007); available for MAVEN but
 454 not MEX) for 10–120 *nm* wavelengths, and for MEX from the solar 10.7 *cm* radio flux
 455 index extrapolated to Mars assuming a $1/r_{Mars Sun}^2$ law. Using solar radio flux values for
 456 MAVEN leads to almost identical results, since both parameters are strongly correlated
 457 (with a correlation factor of 0.98 (n)). However, we choose the FISM model for MAVEN
 458 since it is slightly more precise than the radio flux proxy (FISM uses data and a num-
 459 ber of proxies including the radio flux proxy, selecting the most appropriate information
 460 for each wavelength at each time). Moreover, the absolute values of EUV are of no in-
 461 terest in our case since we only focus on variabilities and correlations.

462 Figure 5b shows a MEX EUV distribution that is roughly uniform with regards to
 463 the angular distance from the strongest crustal source region or to ϕ_{mso} , with also more
 464 frequent low EUV fluxes than high fluxes. In contrast, the MAVEN EUV distribution
 465 (Figure 5a) reveals the presence of two separate regimes, one low and one high regime
 466 (with a difference of almost a factor of 2), corresponding to time periods before (high
 467 EUV fluxes) and after (low EUV fluxes) spring 2015. Moreover, the low MAVEN EUV
 468 fluxes mainly occurred when the spacecraft was away from the strongest crustal source
 469 region, while high EUV fluxes occurred close to the strongest crustal source region. Con-
 470 sequently, the EUV mean profile vs the angular distance to the strongest crustal source
 471 region is similar to the MAVEN mean profile of the BS distance (in Figure 3a). The in-
 472 terpretation of the crustal field influence on the BS distance from Figure 3 may thus be
 473 biased by the inhomogeneous EUV distribution induced by the evolution of the orbit of
 474 the spacecraft while the Sun activity decreased from 2014 to 2017. A similar bias also
 475 appears regarding the EUV profile vs ϕ_{mso} (panels c vs d), with a clear peak at noon sim-
 476 ilar to the peak observed for the MAVEN BS location in Figure 4. Both biases are re-
 477 lated to the orbital precession of the MAVEN spacecraft. These biases may then increase
 478 artificially the apparent influence of crustal fields in the MAVEN data analysis that ap-
 479 peared stronger than in the MEX case.

480 These biases may also be seen through the linear Pearson correlation factors, on
 481 one side, between the angular distance and the BS extrapolated terminator altitude, and

482 on the other side between the angular distance and the main controlling parameters of
 483 the BS drivers that are a priori the EUV fluxes and magnetosonic mach number (Halekas
 484 et al. (2017)). The MAVEN magnetosonic mach number (Mms) is calculated with the
 485 method by Halekas et al. (2017): $Mms = v_{sw}/\sqrt{c_s^2 + v_A^2}$, with v_{sw} SW speed, c_s sound
 486 speed, v_A Alfvén speed, with the electron temperature assumed equal to the proton tem-
 487 perature and a polytropic index $\gamma = 5/3$. It cannot be calculated for MEX due to the
 488 lack of magnetic field measurements.

489 The linear correlation coefficients show indeed that the angular distance is more
 490 correlated with EUV fluxes for MAVEN (correlation factor -0.34 (n)) than it is with
 491 the BS terminator altitude R_{TD} (correlation factor of -0.24 (n)). The same compari-
 492 son can be done for ϕ_{mso} and its correlation with EUV (correlation factor 0.21 (n)) com-
 493 pared to R_{TD} (correlation factor 0.19 (n)). The situation for MEX is the contrary, thus
 494 confirming the absence of bias in the MEX case. We note that the Mms does not in-
 495 troduce a significant bias, with for MAVEN small correlations between the angular dis-
 496 tance and the Mms (correlation factor of 0.04 with a large p-value above 1%) compared
 497 to the correlation between angular distance and R_{TD} .

498 As a consequence, a part of the MAVEN observed dependence of the BS distance
 499 on the angular distance or the MSO longitude of the strongest crustal source region is
 500 probably due to the cross-correlations of these parameters with EUV (see below the par-
 501 tial correlation analysis for a better understanding of the influence of this cross-correlation).
 502 These biases may have influenced the results obtained by Gruesbeck et al. (2018) who
 503 showed strong hemispheric differences of their 3D modeled BS, either regarding the North/South
 504 difference or when the strongest crustal source region was on the dayside vs nightside.
 505 More precisely, when focusing around low Solar Zenith Angles (SZAs) in their study, the
 506 EUV fluxes were indeed maximum for low SZAs of the spacecraft and in the southern
 507 hemisphere, leading to a strong north/south asymmetry (> 1000 km) that was only par-
 508 tially caused by the presence of crustal fields. Moreover, we shall add that using the North
 509 vs South asymmetries and attribute them to the crustal field influence (as performed in
 510 a number of studies of the Martian interaction) may be significantly biased by the sea-
 511 sonal change of EUV fluxes sweep between the northern and southern hemispheres dur-
 512 ing the summer and winter solstices. The North vs South asymmetry caused by crustal
 513 fields may thus be overestimated or underestimated depending on the seasons due to the
 514 significant influence of EUV induced ionization. At high (solar EUV) illumination pe-

515 riods of the Martian orbit, one can even observe BS on average further in the northern
 516 hemisphere than in the southern hemisphere.

517 However, these biases impact only the influence of the angular distance and the MSO
 518 longitude to the strongest crustal source region in the case of the MAVEN dataset. They
 519 impact neither the MEX dataset, nor the analysis of Figure 1 for the MAVEN dataset:
 520 there is no correlation between the IAU longitude and the EUV, with a large p-value (35%)
 521 when testing for the linear correlation between the cosine of the IAU longitude and the
 522 EUV (when selecting only the latitudes around the strongest crustal source region).

523 In order to confirm that the influence of the angular distance to the strongest crustal
 524 source region or of its ϕ_{mso} is not due only to the EUV influence in the MAVEN case,
 525 we performed a partial correlation analysis. An approach based on subsets of the whole
 526 dataset was tried at first, by separating low vs strong EUV conditions subsets to remove
 527 its major influence, but this leads to poor coverage of the crustal fields (in angular dis-
 528 tance or crustal field pressure) and can thus not be used to identify the influence of crustal
 529 fields.

530 Table 1 provides the results for a partial correlation analysis of the influence of an-
 531 gular distance and the cosine of ϕ_{mso} on the extrapolated terminator BS altitude (R_{TD}),
 532 after controlling the other main parameters of influence. We here consider as control-
 533 ling parameters the EUV fluxes (for MAVEN/MEX) and magnetosonic mach number
 534 (for MAVEN only) which are known major parameters of influence of the BS location.

535 The partial correlation analysis makes it possible to compare the correlation fac-
 536 tors between two variables before and after controlling for the other considered param-
 537 eters. In the case of MEX, the correlations between R_{TD} and both the angular distance
 538 and the longitude of the strongest crustal source region were only slightly reduced af-
 539 ter controlling for EUV, while for MAVEN they were reduced by a factor 2 after con-
 540 trolling for EUV and Mms, thus reaching the MEX correlation levels (or close to for the
 541 longitude of the strongest crustal source region). This confirms the significant biases for
 542 the MAVEN dataset due to the EUV inhomogeneous distribution with respect to an-
 543 gular distance and longitude of the strongest crustal source region center, as well as the
 544 absence of bias for MEX. In both cases, the t-test statistics t is well above the t_{H_0} value
 545 that corresponds to the null hypothesis for a risk of 5%, corresponding to negligible or
 546 small p-values. Note that the significance levels of independent tests cannot be compared

547 to each other to discuss the relative importance of variables, each test shall be consid-
 548 ered individually.

549 The multiple linear regression used provides a rough estimate of the relative im-
 550 portance of the drivers included in the regression, by comparing the beta-weights (i.e.
 551 magnitudes of the coefficients). These are the slopes associated with each parameter of
 552 influence in the regression model, normalized by the ratio of the standard deviations of
 553 the BS terminator distance and of each parameter. The beta-weight of angular distance
 554 thus appears 3 to 4 times smaller than the EUV beta-weight for both MEX and MAVEN,
 555 suggesting a consistent relative influence that is smaller than EUV. Note that for MAVEN
 556 $\frac{b_{Mms}^*}{b_{ang.dist.}^*} \sim 4.1$ confirming that EUV and *Mms* are major drivers of the BS location. The
 557 beta-weight of ϕ_{mso} appears 3 to 5 times smaller than the beta-weight of EUV (with a
 558 smaller influence for MAVEN). The longitude of the strongest crustal source region cen-
 559 ter appears, based only on correlation coefficients, less than or as influent as the angu-
 560 lar distance to the strongest crustal source region depending on the mission.

561 Note that a partial correlation analysis confirms that the crustal fields located in
 562 the nightside hemisphere have (little or) no influence on the BS location. Partial cor-
 563 relations between the shock location and the local crustal field pressure (after control-
 564 ling for EUV and mach number when available) for MEX and MAVEN, which are sig-
 565 nificant on the dayside despite being smaller than correlations with angular averaged crustal
 566 field pressures, become non significant (with large p-values close to or larger than 5%)
 567 beyond the terminator. Using large scale crustal field parameters (i.e. angular averaged
 568 pressure) instead of the local pressure also leads to reduced apparent influence beyond
 569 the terminator. However, the correlations still appear significant probably because the
 570 large scale parameters integrate to some extent dayside regions as well given the prox-
 571 imity of most of the nightside BS crossings with the terminator region.

572 The exact values of the statistical results shown above depend on the parameters
 573 included in the regression model (number of parameters, various methods to estimate
 574 the crustal magnetic field pressure instead of angular distance...), on the chosen model
 575 (linear or power law), or on the conic parameters used to derive the R_{TD} altitudes, but
 576 the conclusions remain unchanged: the angular distance or crustal magnetic field pres-
 577 sure integrated over an angular range as well as the MSO longitude of the strongest crustal
 578 source region are significant drivers of the BS terminator distance - despite a bias in the

579 MAVEN case due to the EUV distribution - , and EUV/Mms appear as the major drivers
580 for the BS location.

581 We have in particular checked the robustness of the results by using different datasets
582 (for example only the Gruesbeck et al. (2018) list or only the XF17 list) and various conic
583 fit parameters (i.e. the parameters by Edberg et al. (2008), Hall et al. (2016b), XF17 for
584 either MAVEN or MEX): except for slightly different absolute altitudes, all results dis-
585 cussed above are unchanged.

586 The results show that empirical models representing the BS location should include
587 the crustal fields whose influence is thus significant despite being of smaller importance
588 compared to EUV or mach number. A detailed analysis of the best functional form of
589 the shock location combining all the BS location drivers is beyond the scope of this pa-
590 per, but one can provide a simple empirical proxy that reflects the apparent influence
591 of crustal fields with respect to EUV and mach number based on our study. If one as-
592 sumes a power law relation for the main drivers (EUV and mach number for MAVEN)
593 and for crustal fields, one can derive power index values of each driver. For example, con-
594 sidering a simple relation such as $R_{TD} = a * K^{1/6} + b$ with a/b free constants and K
595 a composite parameter defined by $K = EUV/(Mms * Ang_{dist}^{1/3})$ (without the Mms pa-
596 rameter for MEX due to the absence of magnetic field) leads to correlation coefficients
597 of 0.65/0.41 (n) for the MAVEN/MEX datasets, which are very strong correlation co-
598 efficients given the large amount of data. The 1/3 ratio is approximate but gives an or-
599 der of magnitude of the relative influence of the EUV/mach/crustal field drivers as given
600 by a classic multivariate regression, or by partial correlation analysis (see e.g. table 1)
601 that provide slope ratios for specific drivers (with a slope ratio $\frac{b_{EUV}^*}{b_{Mms}^*}$ close to 1, and $\frac{b_{EUVorMms}^*}{b_{ang.dist}^*}$
602 around 3). Note that using power law or linear forms, or angular averaged crustal field
603 pressure instead of angular distance to the strongest crustal field region, do not change
604 these qualitative results.

605 This type of composite parameter is representative of the overall behavior of the
606 shock location, but other drivers not studied in this paper shall be studied as well, such
607 as the solar wind dynamic pressure, as well as the IMF intensity and orientation param-
608 eters. Moreover, investigating the relative influences in a complex system where numer-
609 ous possible drivers can influence the BS location and can be cross correlated shall be
610 performed with the use of specific techniques, as investigated in a forthcoming paper.

Table 1. Partial correlation analysis for the angular distance to and location of the strongest crustal source region

Statistical parameters	MAVEN	MEX
Direct correlation coefficient R_{TD} vs angular distance (p-value)	-0.24 (n ¹)	-0.12 (n)
Controlled correlation coefficient R_{TD} vs angular distance (p-value)	-0.12 (n)	-0.11 (n)
Significance ratio t/t_{H_0} for angular distance	3.47	6.10
Relative influence $\frac{b_{EUV}^*}{b_{ang.dist.}^*}$	-3.73	-2.90
Direct correlation coefficient R_{TD} vs $\cos(\phi_{mso}^2)$ (p-value)	0.19 (n)	0.12 (n)
Controlled correlation coefficient R_{TD} vs $\cos(\phi_{mso})$ (p-value)	0.09 (n)	0.11 (n)
Significance ratio t/t_{H_0} for $\cos(\phi_{mso})$	2.71	6.19
Relative influence $\frac{b_{EUV}^*}{b_{\cos(\phi_{mso})}^*}$	5.22	2.85

¹ "n" refers to negligible p-values ($< 10^{-5}$)

² ϕ_{mso} refers to the MSO longitude of the strongest crustal source region center

4 Discussion

Beyond the analysis of the global influence of crustal fields on the BS location, one can also investigate the seasonal variability of this influence. Figure 6 shows the compared seasonal variation of several parameters based on the Mars Express dataset that covered 6 martian years. We chose to focus on the Mars Express dataset that is more reliable than our MAVEN dataset that covers less than one martian year. The figure shows first how the influence of the strongest crustal field region on the MEX BS location varies with the solar longitude. The specific influence of the strongest crustal field region shown in the figure is defined as follows: we consider the crossings in the southern hemisphere latitude band of $\pm 20^\circ$ around the latitude of the strongest crustal field region center assumed at -45° , that was used in Section 3.1 to reveal a longitude modulation of the BS location; we then calculate the difference $R_{TD,closemean} - R_{TD,awaymean}$ between the mean R_{TD} altitudes of the BS crossings close (120–240 degrees East longitude range, see Figure 3d) vs away (0–120 and 240–360 degrees East longitude) from the main source center located at $\sim 180^\circ$ East longitude.

626 Figure 6 shows first that this R_{TD} difference is always positive, which is coherent
 627 with the strongest crustal field region pushing the BS further, with up to 400 km alti-
 628 tude difference. The figure also shows that the R_{TD} difference is maximum from about
 629 $Ls \sim 150^\circ$ to $Ls \sim 250^\circ$, i.e. from slightly before equinox until perihelion. The R_{TD}
 630 difference then shows a minimum around perihelion, at a period where the northern hemi-
 631 sphere is the most illuminated. Most of the crustal field sources are located in the south-
 632 ern hemisphere that is the most illuminated at the periods where the R_{TD} difference is
 633 maximum, which suggests a coupling with the ionosphere. The absolute R_{TD} altitude
 634 of the BS is expected to vary with the solar longitude due to the direct influence of ion-
 635 ization of the atmosphere, thus increasing the size of the obstacle through e.g. pickup
 636 ions and currents. However, one does not expect a priori a seasonal variability inside a
 637 given southern hemisphere latitude band between regions close and away from the main
 638 crustal field source region, unless a coupling exists between the ionosphere and the crustal
 639 fields influence on the BS.

640 The figure also provides the seasonal variability of the Total Electron Content given
 641 by the MEX MARSIS instrument, showing in a similar manner the TEC difference ($TEC_{close,mean} -$
 642 $TEC_{away,mean}$) between regions close vs away from the strongest crustal field region in the
 643 southern latitude band $\pm 20^\circ$ around the center latitude -45° . The dataset, already an-
 644 alyzed in detail by Sánchez-Cano et al. (2021), is made of all TEC observations by MAR-
 645 SIS from Martian year 27 until Martian year 32.

646 One thus observes a strong correlation between the seasonal variability of the BS
 647 R_{TD} difference and the seasonal variability of the ionospheric TEC difference. Both pro-
 648 files exhibit similar trends, with minima and maxima at the same seasons, in accordance
 649 with results by Sánchez-Cano et al. (2018). This strong correlation thus suggests that
 650 the seasonal variability of the influence of the strongest crustal field region on the BS
 651 is associated with the seasonal variability of the ionosphere. This confirms the presence
 652 of significant coupling processes between crustal fields and the ionosphere, and conse-
 653 quently with the BS location. The TEC is known to be a good tracer for not only the
 654 ionospheric variability, due to solar irradiance that is the major ionization source of the
 655 sunlit ionosphere, but also for the thermosphere-ionosphere coupling and possibly for the
 656 lower-upper atmosphere coupling. Several studies showed evidence for a coupling between
 657 the ionosphere and the crustal fields, resulting in increased ionospheric electron density
 658 - by 20% to 50% - and reduced temperature in these regions (González-Galindo et al.

(2021), Flynn et al. (2017)). The density increase observed above crustal field regions was attributed to stable mechanisms instead of transient phenomena such as solar flares or enhanced particle precipitation. Ions newly formed by photoionization could be inhibited from diffusing out of the regions with strong crustal fields, resulting in higher densities (Duru et al. (2019)) despite the stable ionization efficiencies in these regions (Lillis et al. (2021)). Electrons trapped on closed field lines are indeed protected against loss mechanisms induced by the magnetosheath plasma and solar wind interaction, which leads to larger lifetimes and densities. The crustal fields thus impact the ionosphere characteristics, which then increases the local ionospheric pressure, and may push further the bow shock due to pressure enhancement and due to the inflation of the apparent obstacle to solar wind via magnetosonic waves. For instance, the ionopause is known to be affected by the presence of crustal fields, with fewer ionopause detections over crustal fields since the increased local pressure (thermal + magnetic) makes it difficult for the SW dynamic pressure to penetrate, compress the ionosphere and form the ionopause (Sánchez-Cano et al. (2020)).

The results above show that the coupling between crustal fields and the ionosphere plays a significant role in the influence of crustal fields on the BS location described in the previous sections. However, it remains difficult to conclude whether this coupling is the dominant process that takes place regarding the influence of crustal fields on the BS location, in addition to other processes such as the magnetic pressure enhancement due to crustal fields and the induced draping topology modification. This coupling has probably also a significant influence on the other plasma boundaries such as the Induced Magnetospheric Boundary or the PhotoElectron Boundary which tightly depend on internal drivers. Further work will be performed to better characterize the complex coupling mechanisms that link the crustal fields to the TEC and ionosphere (and thus to the thermosphere) and to the induced magnetosphere up to the BS.

5 Conclusions

The recent studies of the Martian environment, thanks in particular to the MEX and MAVEN missions, underline the strong and complex influence of the crustal magnetic fields on the Martian environment and its interaction with the solar wind. Among them is the influence on the dynamic plasma boundaries that shape this interaction and on the bow shock (BS) in particular. Compared to other drivers of the BS location (e.g.

691 SW dynamic pressure, extreme ultraviolet fluxes...), the crustal magnetic fields are poorly
692 understood, with in the literature essentially differences observed between the southern
693 and northern hemispheres attributed to the crustal fields, and an influence that ranges
694 from little or no impact to strong influence depending on the authors and on the meth-
695 ods used. We analyzed in this paper in detail the influence of the crustal fields on the
696 BS location, based on a one-dimensional approach using the extrapolated terminator dis-
697 tance of the shock crossings. This lead to the following results :

- 698 • our study provides the first multi-mission detailed analysis of the poorly under-
699 stood influence of the crustal fields on the Martian BS location, by studying datasets
700 from two different spacecraft (MAVEN and MEX, including $> 15,000$ shock cross-
701 ings) and using several methods that provide a coherent picture instead of single
702 point of views eventually contradictory as in previous works
- 703 • the crustal field sources on the Martian surface induce an influence on the BS lo-
704 cation that is maximum when considering crustal field intensities or pressures (or
705 even power law values of it) averaged an angular range of $70 - 80^\circ$, slightly less
706 than a hemispheric asymmetry
- 707 • a number of crustal field source regions can play a role, from few nT intensity at
708 a reference altitude of 400 km
- 709 • however, the strongest crustal field region in the southern hemisphere appears as
710 the dominant driver
- 711 • we introduce the angular distance to the strongest crustal field region, which bet-
712 ter reveals the influence of this region that is shown to extend between at least
713 $40 - 60^\circ$ angular distance (which is consistent with the size of this region) and
714 a full hemisphere
- 715 • this influence may also be seen through the modulation of the BS location by a
716 longitude modulation when focusing around southern latitudes (which reveals a
717 stronger modulation than if all latitudes are included as in previous studies)
- 718 • the crustal field influence is all the more reduced than the strongest crustal source
719 region is located far from the noon direction, with a strong sinusoidal modulation
720 by the local time of the strongest source region. This modulation is probably due
721 to an increased travel time and attenuation for the magnetosonic wave until the
722 solar wind upstream of the planet, combined with an expected larger Alfvén ve-
723 locity in the dayside draping region where the magnetic field increases

- 724 • our analysis suggests that the crustal fields have no (eventually little) influence
725 beyond the terminator region
- 726 • the influence of the strongest crustal field region appears more clearly when the
727 IMF is stable during the preceding hours: the IMF usually rotates at short timescales,
728 while the influence of the crustal fields is essentially a geographical influence in
729 the planetary frame with a much larger timescale, which may partially mask its
730 influence on the distant BS due to the rotation of the solar wind interaction
- 731 • we introduce a technique, i.e. partial correlations (Baba et al. (2004)), that allows
732 to quantify the influence of second order importance drivers which may be hid-
733 den by the influence of correlated major drivers ; this approach appears necessary
734 to provide a coherent picture when considering several mission datasets (MAVEN
735 and MEX) where cross correlations exist (in particular for MAVEN), and it con-
736 firms the significant influence of the crustal fields on the Martian BS location
- 737 • we show the existence of a bias in the MAVEN data (but not in the MEX data)
738 that leads to an incorrect estimation of the crustal field influence when authors
739 focus only on north vs south hemispheric asymmetries during the same period of
740 our dataset (2014-2017), since this asymmetry depends significantly on EUV con-
741 ditions
- 742 • the partial correlation approach confirms that EUV and magnetosonic mach num-
743 ber are major drivers of the BS location, while crustal fields are a significant but
744 a second order driver of this boundary, with an induced variability of the order
745 of several hundreds of km
- 746 • we provide a composite simple parameter that is representative of the overall be-
747 havior of the shock location with respect to EUV, magnetosonic mach number and
748 crustal fields, in a coherent manner for both MAVEN and MEX datasets
- 749 • we show the existence of a seasonal variability of the influence of the strongest crustal
750 field region on the BS
- 751 • moreover, the seasonal variability of the crustal field influence is strongly corre-
752 lated to the Total Electronic Content that is a tracer for the ionosphere dynam-
753 ics and for its coupling with the thermosphere ; our results reveal the existence
754 of a large scale coupling between the crustal fields, the ionosphere and the BS (and
755 probably with other plasma boundaries), presumably due to a density increase fol-

756 lowing the trapping of plasma on the closed field lines thus protected against loss
757 mechanisms induced by the solar wind interaction

758 Our study thus confirms the significant influence of crustal fields on the BS loca-
759 tion based on a multi-mission analysis, describes in detail how this influence takes place
760 (planetary longitude modulation, local time of and angular distance to the strongest crustal
761 field region, crustal field pressure minimum threshold), and quantifies its spatial extent
762 as well as its impact in terms of altitude of the BS. It also sheds a new light on the com-
763 plexity of the influence of crustal fields on the martian environment, with an impact on
764 the BS that is shown to be tightly coupled to both the ionosphere below (and possibly
765 to the thermosphere through the TEC correlation observed) and to the IMF above that
766 can modulate this influence through its rotation. This shows again how the martian en-
767 vironment is a complex fully connected system, where crustal fields make Mars a unique
768 case.

769 In the future we also plan to investigate the use of artificial intelligence techniques
770 to provide automatic catalogs of plasma boundaries and eventually identify complex non
771 linear relationships between the boundaries location and external/internal drivers. These
772 techniques are mature and proved efficient in space physics to detect plasma phenom-
773 ena (see e.g. Karimabadi et al. (2009), Nguyen et al. (2019)) or to identify parameters
774 of influence (see e.g. Al-Ghraibah, A. et al. (2015), Benvenuto et al. (2018), Lenouvel
775 et al. (2021)).

776 **Appendix A Partial correlation approach**

777 The partial correlation approach (Baba et al. (2004)) investigates multiple regres-
778 sions, calculating the correlation coefficients - and estimate their significance - between
779 e.g. two variables y and x_0 , after controlling for the influence of other variables x_i . The
780 correlations are assumed linear ($y = a + \sum_i x_i \cdot b_i$ with b_i constant individual slopes
781 and a constant), but can correspond to power law relations of the type $y = a \prod_i x_i^{b_i}$ since
782 the logarithm of the expression linearizes the expression.

783 For example, if one considers only three variables that are possibly correlated (x ,
784 y , z), the partial correlation between x and y , after controlling for z , is calculated as fol-
785 lows: first the linear regression between x and z is performed, and the residuals are given
786 by the difference between the x values and the regression. Subtracting the regression line

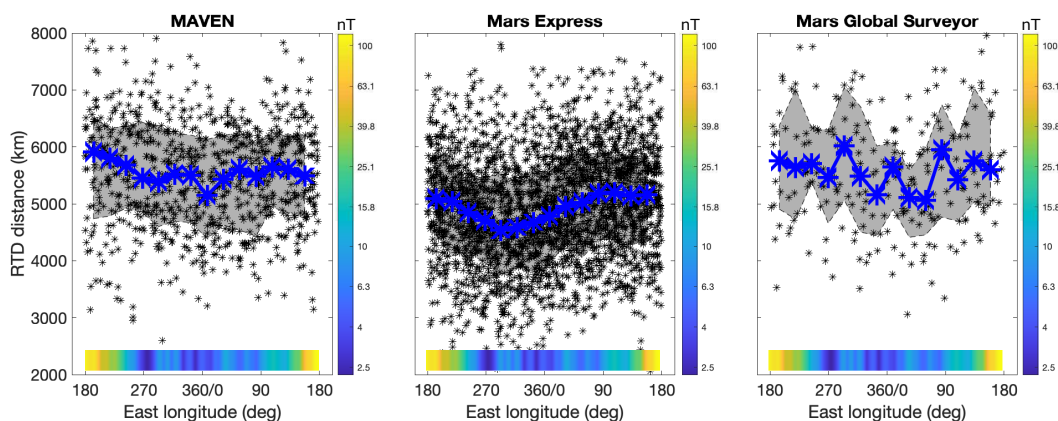


Figure 1. Geographical longitude modulation of the shock terminator altitude for all crossings (points) or the median profile (line), for the shock datasets from MAVEN (left panel), Mars Express (middle panel) and Mars Global Surveyor (right panel). Only crossings that occurred at latitudes inside a $\pm 20^\circ$ latitude band around the strongest crustal source region (assumed centered around $\sim -45^\circ$ latitude and $\sim 180^\circ$ longitude) were considered. The shaded area covers the 20% to 80% percentiles range of shock terminator altitudes. The colorbar shows the longitude modulation of the crustal magnetic field intensity (logarithmic scale, in nT) from the Morschhauser et al. (2014) model at 400 km altitude, averaged over 1° longitude bins in the $\pm 20^\circ$ latitude band.

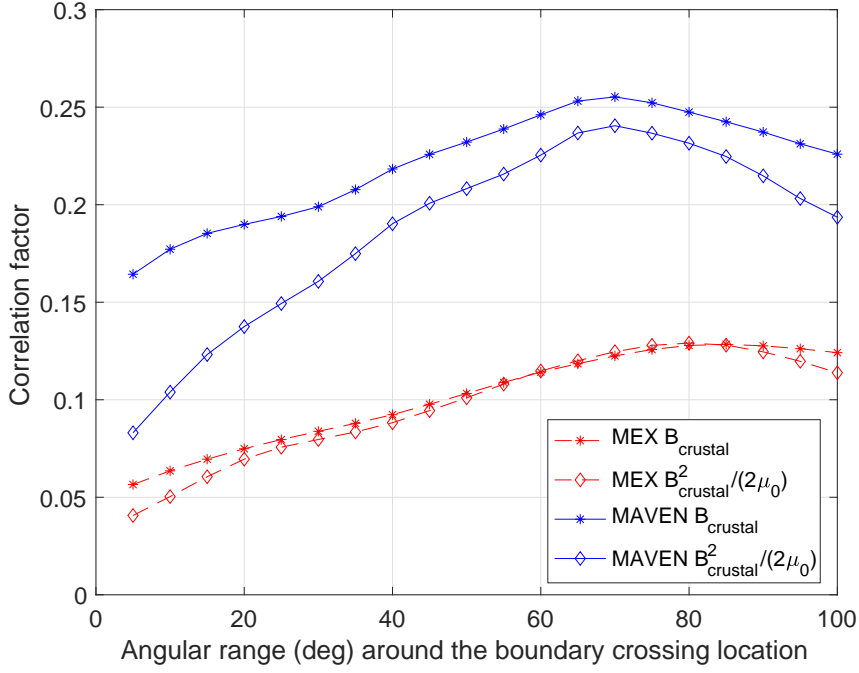


Figure 2. Correlation factor between the R_{TD} terminator altitude of the shock crossings (for MAVEN in blue, for Mars Express in red) and crustal magnetic field pressure or intensity. The crustal field magnetic field intensity or pressure are taken from the Morschhauser et al. (2014) model at 400 km altitude at the sub-spacecraft position (same IAU longitude and latitude) below the crossing, then averaged over an angular range around the sub-spacecraft location. The correlation factor is given as a function this angular range, to reveal whether the crustal field influence on the shock location is local or global.

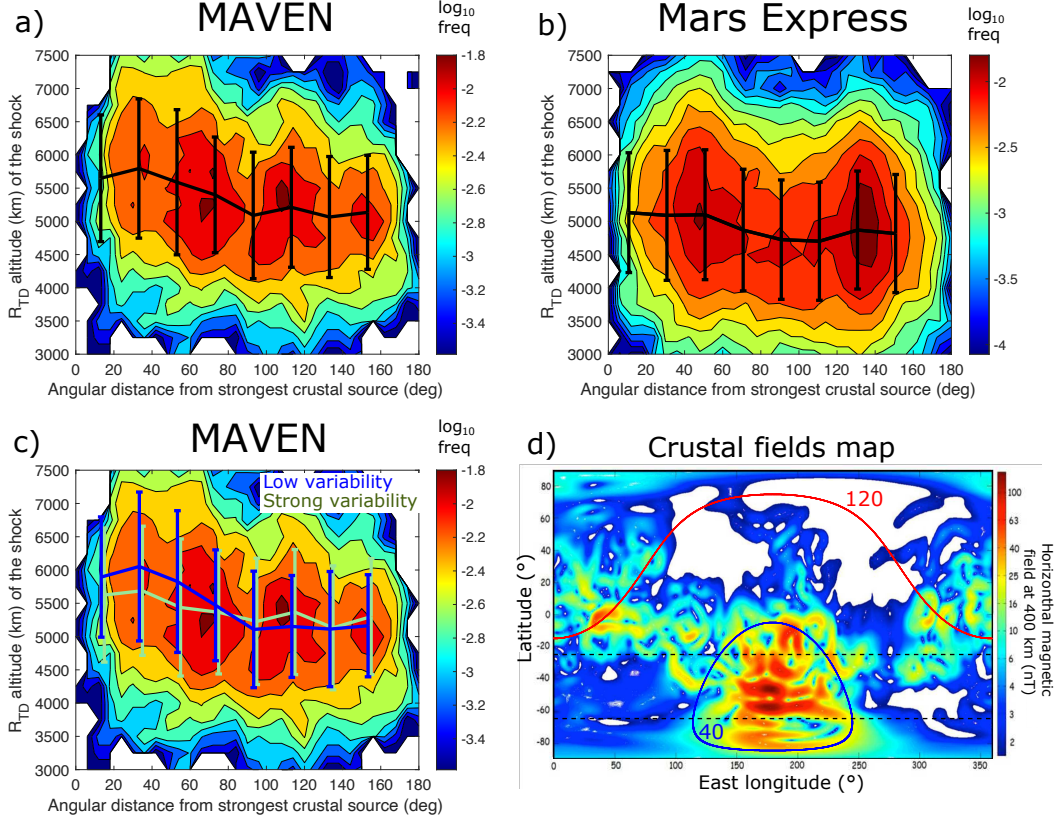


Figure 3. Logarithmic occurrence frequency of the shock crossings distributions for the MAVEN (panel a and c) and Mars Express (panel b) datasets as a function of the terminator altitude and of the angular distance from the strongest crustal source region center (see text for details). The mean and standard deviation are superimposed. Panel c: same distribution as panel a, with means and standard deviations for either low or strong IMF clock angle orientation variabilities preceding the BS crossings. Panel d: geographical map of the horizontal crustal magnetic field at 400 km altitude, with isocontours of the angular distance from the strongest crustal source region (blue line for 40° , red line for 120°) and two isolatitude lines at -25° and -65° .

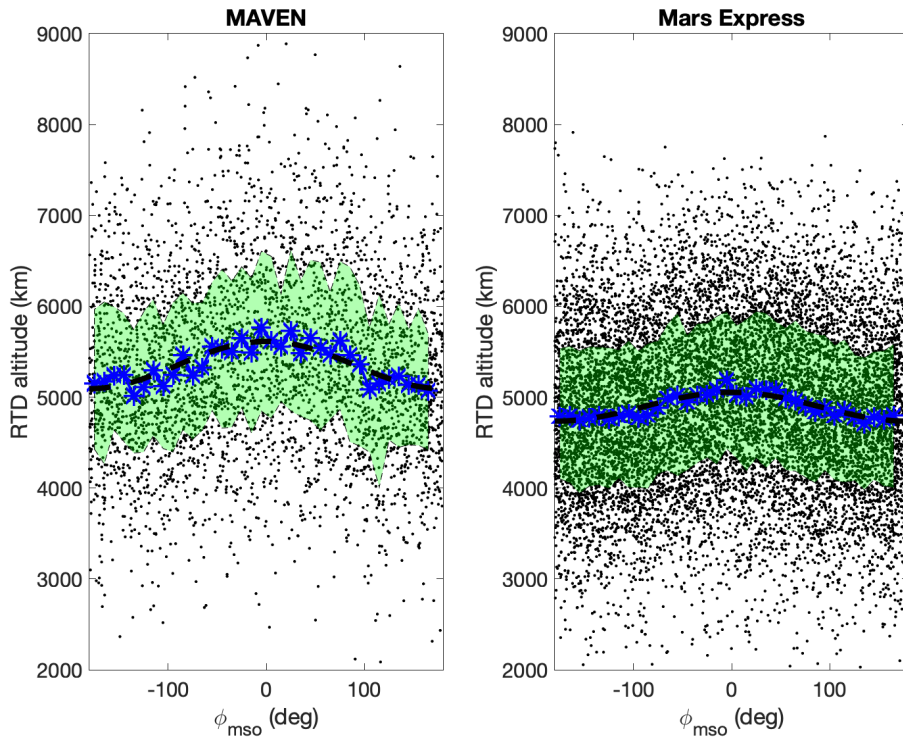


Figure 4. MAVEN (left) and Mars Express (right) shock R_{TD} terminator altitude as a function of ϕ_{mso} the MSO longitude of the strongest crustal source region center: 0° at noon, $+90^\circ$ at dusk -90° at dawn. The mean observed profile (blue stars) is compared with a simple cosine fitting (black dashed line). The shaded area covers the 20% to 80% percentiles range of shock terminator altitudes.

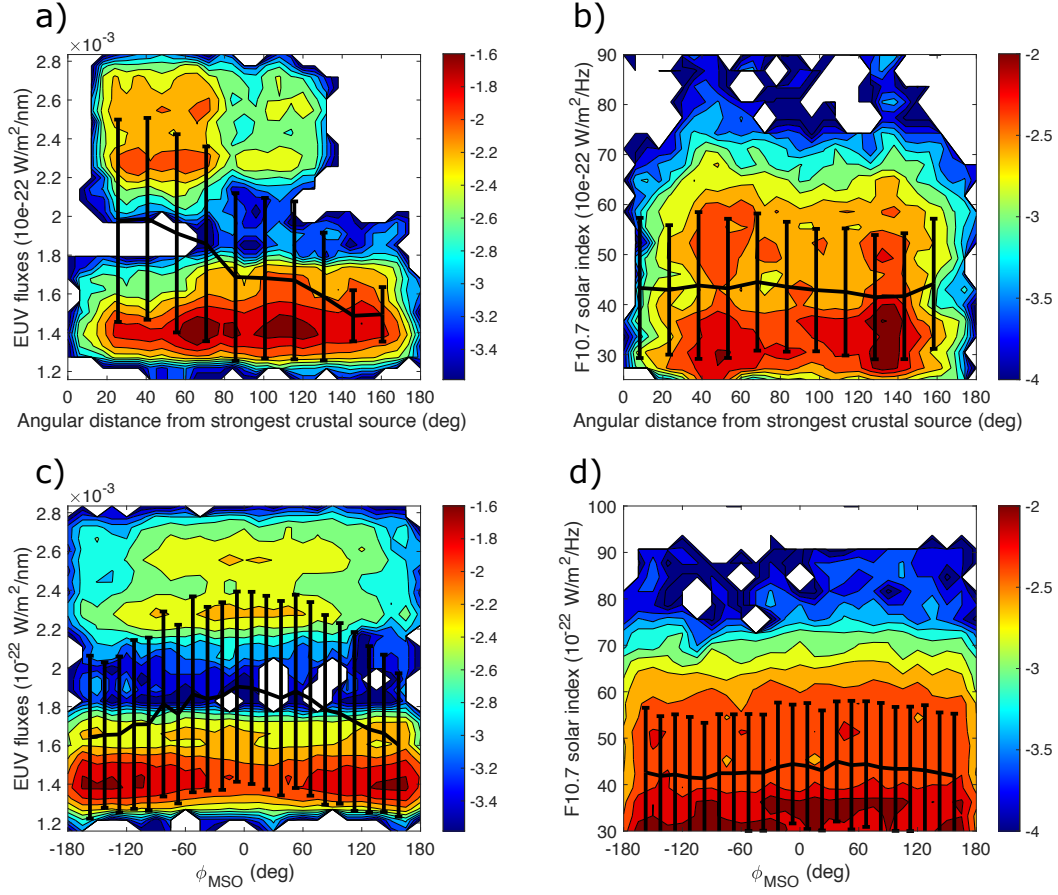


Figure 5. Logarithmic occurrence frequency of the shock crossings distributions for the MAVEN (left panels a and c) and Mars Express (right panels b and d) datasets as a function of the extreme ultraviolet fluxes (given by the FISM EUV fluxes for MAVEN and by the solar 10.7 *cm* radio flux index extrapolated to Mars for Mars Express) and of 1) either the angular distance from the strongest crustal source region (upper panels a and b) 2) or ϕ_{mso} the MSO longitude of the strongest crustal source region (lower panels c and d). The mean and standard deviation are superimposed.

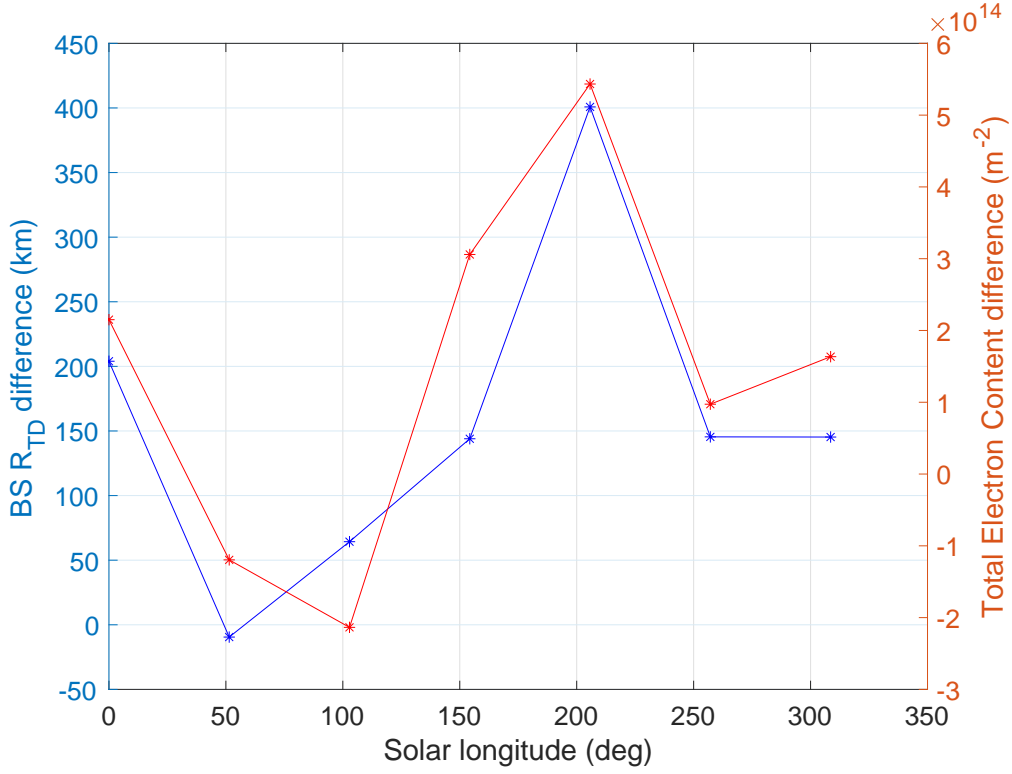


Figure 6. Compared seasonal variation of both the Total Electronic Content (TEC) of Mars ionosphere given by MEX MARSIS data, and of the MEX BS R_{TD} extrapolated terminator altitudes. For both parameters at each season, we show the difference between the value close vs away the strongest crustal field source region (when only focusing on the southern hemisphere $\pm 20^\circ$ latitude band considered in Figure 1 ; see text for more details). The solar longitude (L_s) of Mars is the Mars-Sun angle measured from the Northern Hemisphere spring equinox where $L_s = 0^\circ$ ($L_s = 90^\circ$ corresponds to northern summer solstice, $L_s = 180^\circ$ to northern autumn equinox).

787 removes the influence of z on x . Residuals are then calculated for y with same proce-
 788 dure to remove the influence of z on y . The partial correlation coefficient between x and
 789 y , after controlling for the third variable z , is simply determined by the Pearson corre-
 790 lation coefficients between the two residuals. This technique can be generalized to a larger
 791 number of variables controlled.

The Pearson correlation coefficient between variables x_0 and y controlling for vari-
 ables x_i ($i > 0$) are calculated recursively. The $i + 1$ order partial correlation coeffi-
 cient is given by:

$$r_{x_0 y . x_1 \dots x_i x_{i+1}} = \frac{r_{x_0 y . x_1 x_2 \dots x_i} - r_{x_0 x_{i+1} . x_1 x_2 \dots x_i} \cdot r_{y x_{i+1} . x_1 x_2 \dots x_i}}{\sqrt{1 - r_{x_0 x_{i+1} . x_1 x_2 \dots x_i}^2} \cdot \sqrt{1 - r_{y x_{i+1} . x_1 x_2 \dots x_i}^2}} \quad (\text{A1})$$

792 In order to evaluate the significance of the partial correlation factors with respect
 793 to the null hypothesis H_0 (i.e. null correlation), the test statistics $t = \frac{r}{\sqrt{\frac{1-r^2}{n-3}}}$ is calcu-
 794 lated. For a risk α (e.g. 5% in our case), the null hypothesis is rejected if $|t| > t_{H_0}$
 795 where $t_{H_0} = t_{1-\alpha/2}(n-3)$ is the quantile of order $1 - \alpha/2$ of the Student law for $(n -$
 796 $3)$ degrees of freedom. Similar to classic correlation coefficients, two-sided p-values can
 797 be determined to provide a probability that the null hypothesis is true: i.e. the partial
 798 correlation is not significantly different from 0 as soon as the p-value is larger than the
 799 risk defined (5%).

Moreover, the quality evaluation of regression models, usually given by the deter-
 mination coefficient R^2 , monotonically increases with the number of variables included
 in the model. One thus needs to calculate the adjusted determination coefficient R'^2 to
 compare regression models including more or less variables, with:

$$R'^2 = 1 - \frac{n-1}{n-p-1}(1-R^2) \quad (\text{A2})$$

800 with n number of observations and p number of variables in the regression model, and
 801 $R^2 = 1 - SSE/SST$ with SSE the sum of squared error ($SSE = \sum_i (y_{i_{model}} - y_{mean})^2$)
 802 and SST the sum of squared total ($SST = \sum_i (y_i - y_{mean})^2$).

803 Finally, the individual slopes b_i of variables x_i can be transformed into standard-
 804 ized slopes called beta-weights (b_i^*) enabling to compare the relative influence of the vari-
 805 ables (to avoid e.g. comparing different units or ranges): $b_i^* = b_i \frac{s_i}{s_y}$ with s_i and s_y the
 806 standard deviations of variables x_i and y .

Acknowledgments

This work was supported by the French space agency CNES. The authors acknowledge the support of the MAVEN and Mars Express instrument and science teams, as well as are the CDDP/AMDA team and E. Penou. B.S.-C acknowledges support through UK-STFC Ernest Rutherford Fellowship ST/V004115/1 and UK-STFC consolidated grant ST/S000429/1 and ST/W00089X/1. X.F acknowledges support through NASA grant 80NSSC19K0562. The MGS, MEX and MAVEN datasets of shock crossings are available in the <https://doi.org/10.5281/zenodo.6240624> repository. All MGS, MEX and MAVEN instruments calibrated data are available on the AMDA web interface (<http://amda.cdpp.eu>, in the directory /Parameters/Resources/AMDA Database) as well as on the NASA Planetary Data System (https://pds-atmospheres.nmsu.edu/data_and_services/atmospheres_data/MAVEN/maven_main.html and <https://pds-geosciences.wustl.edu/missions/mgs/index.htm>) for MAVEN and MGS, and in the Planetary Science Archive (<https://www.cosmos.esa.int/web/psa/mars-express>) for MEX, with in particular the MARSIS data available at <https://archives.esac.esa.int/psa/ftp/MARS-EXPRESS/MARSIS/>.

References

- Acuña, M. H., Connerney, J. E. P., Wasilewski, P., Lin, R. P., Anderson, K. A., Carlson, C. W., ... Ness, N. F. (1992). Mars observer magnetic fields investigation. *Journal of Geophysical Research: Planets*, *97*(E5), 7799-7814. Retrieved from <https://agupubs.onlinelibrary.wiley.com/doi/abs/10.1029/92JE00344> doi: <https://doi.org/10.1029/92JE00344>
- Acuña, M. H., Connerney, J. E. P., Wasilewski, P., Lin, R. P., Mitchell, D., Anderson, K. A., ... Ness, N. F. (2001, Oct). Magnetic field of Mars: Summary of results from the aerobraking and mapping orbits. *Journal of Geophysical Research*, *106*(E10), 23403-23418. doi: [10.1029/2000JE001404](https://doi.org/10.1029/2000JE001404)
- Al-Ghraibah, A., Boucheron, L. E., & McAteer, R. T. J. (2015). An automated classification approach to ranking photospheric proxies of magnetic energy build-up. *Astronomy and Astrophysics*, *579*, A64. Retrieved from <https://doi.org/10.1051/0004-6361/201525978> doi: [10.1051/0004-6361/201525978](https://doi.org/10.1051/0004-6361/201525978)
- Alexander, C. J., Luhmann, J. G., & Russell, C. T. (1986). Interplanetary field con-

- 839 trol of the location of the venus bow shock: Evidence for comet-like ion pickup.
840 *Geophysical Research Letters*, 13(9), 917-920. Retrieved from [https://](https://agupubs.onlinelibrary.wiley.com/doi/abs/10.1029/GL013i009p00917)
841 agupubs.onlinelibrary.wiley.com/doi/abs/10.1029/GL013i009p00917
842 doi: <https://doi.org/10.1029/GL013i009p00917>
- 843 Anderson, R. B., & Bell, J. F. (2013). Correlating multispectral imaging and
844 compositional data from the mars exploration rovers and implications for
845 mars science laboratory. *Icarus*, 223(1), 157-180. Retrieved from [https://](https://www.sciencedirect.com/science/article/pii/S0019103512004836)
846 www.sciencedirect.com/science/article/pii/S0019103512004836 doi:
847 <https://doi.org/10.1016/j.icarus.2012.11.029>
- 848 Baba, K., Shibata, R., & Sibuya, M. (2004). Partial correlation and conditional cor-
849 relation as measures of conditional independence. *Australian & New Zealand*
850 *Journal of Statistics*, 46(4), 657-664. Retrieved from [https://onlinelibrary](https://onlinelibrary.wiley.com/doi/abs/10.1111/j.1467-842X.2004.00360.x)
851 [.wiley.com/doi/abs/10.1111/j.1467-842X.2004.00360.x](https://onlinelibrary.wiley.com/doi/abs/10.1111/j.1467-842X.2004.00360.x) doi: [https://doi](https://doi.org/10.1111/j.1467-842X.2004.00360.x)
852 [.org/10.1111/j.1467-842X.2004.00360.x](https://doi.org/10.1111/j.1467-842X.2004.00360.x)
- 853 Barabash, S., Lundin, R., Andersson, H., Brinkfeldt, K., Grigoriev, A., Gunell,
854 H., ... Thocaven, J.-J. (2006). The Analyzer of Space Plasmas and En-
855 ergetic Atoms (ASPERA-3) for the Mars Express Mission. *Space Science*
856 *Reviews*, 126(1), 113-164. Retrieved from [http://dx.doi.org/10.1007/](http://dx.doi.org/10.1007/s11214-006-9124-8)
857 [s11214-006-9124-8](http://dx.doi.org/10.1007/s11214-006-9124-8) doi: 10.1007/s11214-006-9124-8
- 858 Benvenuto, F., Piana, M., Campi, C., & Massone, A. M. (2018, jan). A hybrid
859 supervised/unsupervised machine learning approach to solar flare prediction.
860 *The Astrophysical Journal*, 853(1), 90. Retrieved from [https://doi.org/](https://doi.org/10.3847/1538-4357/aaa23c)
861 [10.3847/1538-4357/aaa23c](https://doi.org/10.3847/1538-4357/aaa23c) doi: 10.3847/1538-4357/aaa23c
- 862 Bertaux, J.-L., Leblanc, F., Witasse, O., Quemerais, E., Lilensten, J., Stern, S. A.,
863 ... Korablev, O. (2005, Jun). Discovery of an aurora on Mars. *Nature*,
864 435(7043), 790-794. doi: 10.1038/nature03603
- 865 Brain, D. A., Lillis, R. J., Mitchell, D. L., Halekas, J. S., & Lin, R. P. (2007,
866 September). Electron pitch angle distributions as indicators of magnetic
867 field topology near Mars. *Journal of Geophysical Research (Space Physics)*,
868 112, A09201. doi: 10.1029/2007JA012435
- 869 Cartacci, M., Amata, E., Cicchetti, A., Noschese, R., Giuppi, S., Langlais, B., ...
870 Picardi, G. (2013). Mars ionosphere total electron content analysis from
871 marsis subsurface data. *Icarus*, 223(1), 423-437. Retrieved from <https://>

872 www.sciencedirect.com/science/article/pii/S0019103512005052 doi:
873 <https://doi.org/10.1016/j.icarus.2012.12.011>

874 Cartacci, M., Snchez-Cano, B., Orosei, R., Noschese, R., Cicchetti, A., Witasse,
875 O., ... Rossi, A. (2018). Improved estimation of mars ionosphere to-
876 tal electron content. *Icarus*, *299*, 396-410. Retrieved from [https://](https://www.sciencedirect.com/science/article/pii/S0019103516306935)
877 www.sciencedirect.com/science/article/pii/S0019103516306935 doi:
878 <https://doi.org/10.1016/j.icarus.2017.07.033>

879 Chamberlin, P. C., Woods, T. N., & Eparvier, F. G. (2007, July). Flare Irradi-
880 ance Spectral Model (FISM): Daily component algorithms and results. *Space*
881 *Weather*, *5*, S07005. doi: 10.1029/2007SW000316

882 Connerney, J. E. P., Espley, J., Lawton, P., Murphy, S., Odom, J., Oliverson, R., &
883 Shepard, D. (2015, December). The MAVEN Magnetic Field Investigation.
884 "*Space Science Reviews*", *195*, 257-291. doi: 10.1007/s11214-015-0169-4

885 Crider, D. H. (2004, Jan). The influence of crustal magnetism on the solar wind in-
886 teraction with Mars: recent observations. *Advances in Space Research*, *33*(2),
887 152-160. doi: 10.1016/j.asr.2003.04.013

888 Dai, Y. S., Wilkes, B. J., Bergeron, J., Kuraszkiewicz, J., Omont, A., Atanas, A., &
889 Teplitz, H. I. (2018, 05). Is there a relationship between AGN and star forma-
890 tion in IR-bright AGNs? *Monthly Notices of the Royal Astronomical Society*,
891 *478*(3), 4238-4254. Retrieved from <https://doi.org/10.1093/mnras/sty1341>
892 doi: 10.1093/mnras/sty1341

893 DiBraccio, G. A., Luhmann, J. G., Curry, S. M., Espley, J. R., Xu, S., Mitchell,
894 D. L., ... Jakosky, B. M. (2018, May). The Twisted Configuration of the
895 Martian Magnetotail: MAVEN Observations. *Geophysical Research Letters*,
896 *45*(10), 4559-4568. doi: 10.1029/2018GL077251

897 Duru, F., Brain, B., Gurnett, D. A., Halekas, J., Morgan, D. D., & Wilkinson, C. J.
898 (2019). Electron density profiles in the upper ionosphere of mars from 11 years
899 of marsis data: Variability due to seasons, solar cycle, and crustal magnetic
900 fields. *Journal of Geophysical Research: Space Physics*, *124*(4), 3057-3066.
901 Retrieved from [https://agupubs.onlinelibrary.wiley.com/doi/abs/](https://agupubs.onlinelibrary.wiley.com/doi/abs/10.1029/2018JA026327)
902 [10.1029/2018JA026327](https://doi.org/10.1029/2018JA026327) doi: <https://doi.org/10.1029/2018JA026327>

903 Edberg, N. J. T., Brain, D. A., Lester, M., Cowley, S. W. H., Modolo, R., Fränz, M.,
904 & Barabash, S. (2009). Plasma boundary variability at mars as observed by

905 mars global surveyor and mars express. *Annales Geophysicae*, 27(9), 3537–
906 3550. Retrieved from [https://angeo.copernicus.org/articles/27/3537/](https://angeo.copernicus.org/articles/27/3537/2009/)
907 2009/ doi: 10.5194/angeo-27-3537-2009

908 Edberg, N. J. T., Lester, M., Cowley, S. W. H., Brain, D. A., Frnz, M., & Barabash,
909 S. (2010). Magnetosonic mach number effect of the position of the bow shock
910 at mars in comparison to venus. *Journal of Geophysical Research: Space*
911 *Physics*, 115(A7). doi: 10.1029/2009JA014998

912 Edberg, N. J. T., Lester, M., Cowley, S. W. H., & Eriksson, A. I. (2008). Statis-
913 tical analysis of the location of the martian magnetic pileup boundary and
914 bow shock and the influence of crustal magnetic fields. *Journal of Geophys-*
915 *ical Research: Space Physics*, 113(A8), n/a–n/a. Retrieved from [http://](http://dx.doi.org/10.1029/2008JA013096)
916 dx.doi.org/10.1029/2008JA013096 (A08206) doi: 10.1029/2008JA013096

917 Fang, X., Liemohn, M. W., Nagy, A. F., Luhmann, J. G., & Ma, Y. (2010, April).
918 Escape probability of Martian atmospheric ions: Controlling effects of the elec-
919 tromagnetic fields. *Journal of Geophysical Research (Space Physics)*, 115(A4),
920 A04308. doi: 10.1029/2009JA014929

921 Fang, X., Ma, Y., Brain, D., Dong, Y., & Lillis, R. (2015). Control of mars
922 global atmospheric loss by the continuous rotation of the crustal mag-
923 netic field: A time-dependent mhd study. *Journal of Geophysical Re-*
924 *search: Space Physics*, 120(12), 10,926–10,944. Retrieved from [https://](https://agupubs.onlinelibrary.wiley.com/doi/abs/10.1002/2015JA021605)
925 agupubs.onlinelibrary.wiley.com/doi/abs/10.1002/2015JA021605 doi:
926 <https://doi.org/10.1002/2015JA021605>

927 Fang, X., Ma, Y., Masunaga, K., Dong, Y., Brain, D., Halekas, J., ... Dong, C.
928 (2017). The mars crustal magnetic field control of plasma boundary locations
929 and atmospheric loss: Mhd prediction and comparison with maven. *Jour-*
930 *nal of Geophysical Research: Space Physics*, 122(4), 4117–4137. Retrieved
931 from [https://agupubs.onlinelibrary.wiley.com/doi/abs/10.1002/](https://agupubs.onlinelibrary.wiley.com/doi/abs/10.1002/2016JA023509)
932 [2016JA023509](https://agupubs.onlinelibrary.wiley.com/doi/abs/10.1002/2016JA023509) doi: 10.1002/2016JA023509

933 Flynn, C. L., Vogt, M. F., Withers, P., Andersson, L., England, S., & Liu, G.
934 (2017). Maven observations of the effects of crustal magnetic fields on elec-
935 tron density and temperature in the martian dayside ionosphere. *Geo-*
936 *physical Research Letters*, 44(21), 10,812–10,821. Retrieved from [https://](https://agupubs.onlinelibrary.wiley.com/doi/abs/10.1002/2017GL075367)
937 agupubs.onlinelibrary.wiley.com/doi/abs/10.1002/2017GL075367 doi:

938 <https://doi.org/10.1002/2017GL075367>

939 Garnier, P., Steckiewicz, M., Mazelle, C., Xu, S., Mitchell, D., Holmberg, M. K. G.,
940 ... Jakosky, B. M. (2017). The martian photoelectron boundary as seen by
941 maven. *Journal of Geophysical Research: Space Physics*, 122(10), 10,472-
942 10,485. Retrieved from <https://agupubs.onlinelibrary.wiley.com/doi/abs/10.1002/2017JA024497> doi: <https://doi.org/10.1002/2017JA024497>

943
944 González-Galindo, F., Eusebio, D., Nmec, F., Peter, K., Kopf, A., Tellmann, S.,
945 & Paetzold, M. (2021). Seasonal and geographical variability of the mar-
946 tian ionosphere from mars express observations. *Journal of Geophysi-
947 cal Research: Planets*, 126(2), e2020JE006661. Retrieved from [https://](https://agupubs.onlinelibrary.wiley.com/doi/abs/10.1029/2020JE006661)
948 agupubs.onlinelibrary.wiley.com/doi/abs/10.1029/2020JE006661
949 (e2020JE006661 2020JE006661) doi: <https://doi.org/10.1029/2020JE006661>

950 Gruesbeck, J. R., Espley, J. R., Connerney, J. E. P., DiBraccio, G. A., Soobiah,
951 Y. I., Brain, D., ... Mitchell, D. L. (2018). The three-dimensional bow
952 shock of mars as observed by maven. *Journal of Geophysical Research: Space
953 Physics*, 123(6), 4542-4555. Retrieved from [https://agupubs.onlinelibrary](https://agupubs.onlinelibrary.wiley.com/doi/abs/10.1029/2018JA025366)
954 [.wiley.com/doi/abs/10.1029/2018JA025366](https://agupubs.onlinelibrary.wiley.com/doi/abs/10.1029/2018JA025366) doi: 10.1029/2018JA025366

955 Halekas, J. S., Ruhunusiri, S., Harada, Y., Collinson, G., Mitchell, D. L., Mazelle,
956 C., ... Jakosky, B. M. (2017, January). Structure, dynamics, and seasonal
957 variability of the Mars-solar wind interaction: MAVEN Solar Wind Ion Ana-
958 lyzer in-flight performance and science results. *Journal of Geophysical Research
959 (Space Physics)*, 122, 547-578. doi: 10.1002/2016JA023167

960 Halekas, J. S., Taylor, E. R., Dalton, G., Johnson, G., Curtis, D. W., McFadden,
961 J. P., ... Jakosky, B. M. (2015, Dec 01). The solar wind ion analyzer for
962 maven. *Space Science Reviews*, 195(1), 125-151. Retrieved from [https://](https://doi.org/10.1007/s11214-013-0029-z)
963 doi.org/10.1007/s11214-013-0029-z doi: 10.1007/s11214-013-0029-z

964 Hall, B. E. S., Lester, M., Nichols, J. D., Sanchez-Cano, B., Andrews, D. J.,
965 Opgenoorth, H. J., & Frnz, M. (2016a). A survey of superthermal electron
966 flux depressions, or electron holes, within the illuminated martian induced
967 magnetosphere. *Journal of Geophysical Research: Space Physics*, 121(5), 4835-
968 4857. Retrieved from [https://agupubs.onlinelibrary.wiley.com/doi/abs/](https://agupubs.onlinelibrary.wiley.com/doi/abs/10.1002/2015JA021866)
969 [10.1002/2015JA021866](https://agupubs.onlinelibrary.wiley.com/doi/abs/10.1002/2015JA021866) doi: <https://doi.org/10.1002/2015JA021866>

970 Hall, B. E. S., Lester, M., Sánchez-Cano, B., Nichols, J. D., Andrews, D. J., Edberg,

- 971 N. J. T., ... Orosei, R. (2016b). Annual variations in the martian bow shock
972 location as observed by the mars express mission. *Journal of Geophysical*
973 *Research: Space Physics*, 121(11), 11,474-11,494. Retrieved from [https://](https://agupubs.onlinelibrary.wiley.com/doi/abs/10.1002/2016JA023316)
974 agupubs.onlinelibrary.wiley.com/doi/abs/10.1002/2016JA023316 doi:
975 10.1002/2016JA023316
- 976 Hall, B. E. S., Sánchez-Cano, B., Wild, J. A., Lester, M., & Holmstrom, M. (2019).
977 The martian bow shock over solar cycle 2324 as observed by the mars express
978 mission. *Journal of Geophysical Research: Space Physics*, 124(6), 4761-4772.
979 Retrieved from [https://agupubs.onlinelibrary.wiley.com/doi/abs/](https://agupubs.onlinelibrary.wiley.com/doi/abs/10.1029/2018JA026404)
980 [10.1029/2018JA026404](https://agupubs.onlinelibrary.wiley.com/doi/abs/10.1029/2018JA026404) doi: 10.1029/2018JA026404
- 981 Kang, W.-Y., Wang, J.-X., Cai, Z.-Y., Guo, H.-X., Zhu, F.-F., Cao, X.-W., ...
982 Yuan, F. (2018, nov). An intrinsic link between long-term UV/optical vari-
983 ations and x-ray loudness in quasars. *The Astrophysical Journal*, 868(1),
984 58. Retrieved from <https://doi.org/10.3847/1538-4357/aae6c4> doi:
985 10.3847/1538-4357/aae6c4
- 986 Karimabadi, H., Sipes, T. B., Wang, Y., Lavraud, B., & Roberts, A. (2009, June). A
987 new multivariate time series data analysis technique: Automated detection of
988 flux transfer events using Cluster data. *Journal of Geophysical Research (Space*
989 *Physics)*, 114, A06216. doi: 10.1029/2009JA014202
- 990 Kim, H.-J., Lyons, L., Boudouridis, A., Pilipenko, V., Ridley, A. J., & Weygand,
991 J. M. (2011). Statistical study of the effect of ulf fluctuations in the imf
992 on the cross polar cap potential drop for northward imf. *Journal of Geo-*
993 *physical Research: Space Physics*, 116(A10). Retrieved from [https://](https://agupubs.onlinelibrary.wiley.com/doi/abs/10.1029/2011JA016931)
994 agupubs.onlinelibrary.wiley.com/doi/abs/10.1029/2011JA016931 doi:
995 <https://doi.org/10.1029/2011JA016931>
- 996 Le, G.-M., & Zhang, X.-F. (2017, dec). Dependence of large SEP events with dif-
997 ferent energies on the associated flares and CMEs. *Research in Astronomy and*
998 *Astrophysics*, 17(12), 123. Retrieved from [https://doi.org/10.1088/1674-](https://doi.org/10.1088/1674-4527/17/12/123)
999 [4527/17/12/123](https://doi.org/10.1088/1674-4527/17/12/123) doi: 10.1088/1674-4527/17/12/123
- 1000 Lenouvel, Q., Génot, V., Garnier, P., Toledo-Redondo, S., Lavraud, B., Aunai, N.,
1001 ... Burch, J. L. (2021, May). Identification of Electron Diffusion Regions with
1002 a Machine Learning Approach on MMS Data at the Earth's Magnetopause.
1003 *Earth and Space Science*, 8(5), e01530. doi: 10.1029/2020EA001530

- 1004 Li, S., Lu, H., Cui, J., Yu, Y., Mazelle, C., Li, Y., & Cao, J. (2020). Effects of a
 1005 dipole-like crustal field on solar wind interaction with mars. *Earth and Plan-*
 1006 *etary Physics*, 4, 23. Retrieved from [http://eppcgs.xml-journal.net//](http://eppcgs.xml-journal.net//article/id/e24b8683-72c4-4300-abdd-0e6899849f0d)
 1007 [article/id/e24b8683-72c4-4300-abdd-0e6899849f0d](http://eppcgs.xml-journal.net//article/id/e24b8683-72c4-4300-abdd-0e6899849f0d) doi: 10.26464/
 1008 epp2020005
- 1009 Lillis, R. J., & Brain, D. A. (2013, Jun). Nightside electron precipitation at
 1010 Mars: Geographic variability and dependence on solar wind conditions.
 1011 *Journal of Geophysical Research (Space Physics)*, 118(6), 3546-3556. doi:
 1012 10.1002/jgra.50171
- 1013 Lillis, R. J., Xu, S., Mitchell, D., Thiemann, E., Eparvier, F., Benna, M., & Elrod,
 1014 M. (2021). Ionization efficiency in the dayside ionosphere of mars: Struc-
 1015 ture and variability. *Journal of Geophysical Research: Planets*, 126(12),
 1016 e2021JE006923. Retrieved from [https://agupubs.onlinelibrary.wiley](https://agupubs.onlinelibrary.wiley.com/doi/abs/10.1029/2021JE006923)
 1017 [.com/doi/abs/10.1029/2021JE006923](https://agupubs.onlinelibrary.wiley.com/doi/abs/10.1029/2021JE006923) (e2021JE006923 2021JE006923) doi:
 1018 <https://doi.org/10.1029/2021JE006923>
- 1019 Ma, Y. J., Fang, X., Nagy, A. F., Russell, C. T., & Toth, G. (2014, February).
 1020 Martian ionospheric responses to dynamic pressure enhancements in the solar
 1021 wind. *Journal of Geophysical Research (Space Physics)*, 119, 1272-1286. doi:
 1022 10.1002/2013JA019402
- 1023 Masunaga, K., Seki, K., Brain, D. A., Fang, X., Dong, Y., Jakosky, B. M., ...
 1024 Eparvier, F. G. (2017, Apr). Statistical analysis of the reflection of inci-
 1025 dent O⁺ pickup ions at Mars: MAVEN observations. *Journal of Geophysical*
 1026 *Research (Space Physics)*, 122(4), 4089-4101. doi: 10.1002/2016JA023516
- 1027 Matsunaga, K., Seki, K., Brain, D. A., Hara, T., Masunaga, K., Mcfadden, J. P.,
 1028 ... Jakosky, B. M. (2017, Sep). Statistical Study of Relations Between the
 1029 Induced Magnetosphere, Ion Composition, and Pressure Balance Boundaries
 1030 Around Mars Based On MAVEN Observations. *Journal of Geophysical Re-*
 1031 *search (Space Physics)*, 122(9), 9723-9737. doi: 10.1002/2017JA024217
- 1032 Mazelle, C., Winterhalter, D., Sauer, K., Trotignon, J. G., Acuña, M. H.,
 1033 Baumgärtel, K., ... Slavin, J. (2004). Bow Shock and Upstream Phe-
 1034 nomena at Mars. *Space Science Reviews*, 111(1), 115-181. doi: 10.1023/B:
 1035 SPAC.0000032717.98679.d0
- 1036 Mitchell, D. L., Lin, R. P., Mazelle, C., Rème, H., Cloutier, P. A., Connerney,

- 1037 J. E. P., ... Ness, N. F. (2001, October). Probing Mars' crustal magnetic
1038 field and ionosphere with the MGS Electron Reflectometer. *Journal of Geo-*
1039 *physical Research*, *106*, 23419-23428. doi: 10.1029/2000JE001435
- 1040 Mitchell, D. L., Mazelle, C., Sauvaud, J.-A., Thocaven, J.-J., Rouzaud, J., Fe-
1041 dorov, A., ... Jakosky, B. M. (2016, April). The MAVEN Solar Wind
1042 Electron Analyzer. *Space Science Reviews*, *200*, 495-528. doi: 10.1007/
1043 s11214-015-0232-1
- 1044 Morschhauser, A., Lesur, V., & Grott, M. (2014, June). A spherical harmonic model
1045 of the lithospheric magnetic field of Mars. *Journal of Geophysical Research*
1046 *(Planets)*, *119*, 1162-1188. doi: 10.1002/2013JE004555
- 1047 Nemec, F., Linzmayer, V., Nemecek, Z., & Safrankova, J. (2020). Martian bow
1048 shock and magnetic pileup boundary models based on an automated region
1049 identification. *Journal of Geophysical Research: Space Physics*, *n/a(n/a)*,
1050 e2020JA028509-T. Retrieved from [https://agupubs.onlinelibrary.wiley](https://agupubs.onlinelibrary.wiley.com/doi/abs/10.1029/2020JA028509)
1051 [.com/doi/abs/10.1029/2020JA028509](https://doi.org/10.1029/2020JA028509) (e2020JA028509-T 2020JA028509-T)
1052 doi: <https://doi.org/10.1029/2020JA028509>
- 1053 Nguyen, G., Aunai, N., Fontaine, D., Le Penneec, E., Van den Bossche, J., Jean-
1054 det, A., ... Regaldo-Saint Blancard, B. (2019, April). Automatic De-
1055 tection of Interplanetary Coronal Mass Ejections from In Situ Data: A
1056 Deep Learning Approach. *The Astrophysical Journal*, *874*(2), 145. Re-
1057 trieved from <https://hal.sorbonne-universite.fr/hal-02103805> doi:
1058 10.3847/1538-4357/ab0d24
- 1059 Ni, Q., Brandt, W. N., Yang, G., Leja, J., Chen, C.-T. J., Luo, B., ... Zhang,
1060 K. (2020, 11). Revealing the relation between black hole growth and
1061 host-galaxy compactness among star-forming galaxies. *Monthly Notices*
1062 *of the Royal Astronomical Society*, *500*(4), 4989-5008. Retrieved from
1063 <https://doi.org/10.1093/mnras/staa3514> doi: 10.1093/mnras/staa3514
- 1064 Poppe, A. R., Brain, D. A., Dong, Y., Xu, S., & Jarvinen, R. (2021, January).
1065 Particle-In-Cell Modeling of Martian Magnetic Cusps and Their Role in En-
1066 hancing Nightside Ionospheric Ion Escape. *Geophysical Research Letters*,
1067 *48*(1), e90763. doi: 10.1029/2020GL090763
- 1068 Romanelli, N., Modolo, R., Leblanc, F., Chaufray, J. Y., Hess, S., Brain, D., ...
1069 Jakosky, B. (2018, Jul). Effects of the Crustal Magnetic Fields and Changes

1070 in the IMF Orientation on the Magnetosphere of Mars: MAVEN Observations
1071 and LatHyS Results. *Journal of Geophysical Research (Space Physics)*, 123(7),
1072 5315-5333. doi: 10.1029/2017JA025155

1073 Sánchez-Cano, B., Lester, M., Cartacci, M., Orosei, R., Witasse, O., Blelly, P.-L.,
1074 & Kofman, W. (2021). Ionosphere of mars during the consecutive solar
1075 minima 23/24 and 24/25 as seen by marsis-mars express. *Icarus*, 114616.
1076 Retrieved from [https://www.sciencedirect.com/science/article/pii/](https://www.sciencedirect.com/science/article/pii/S0019103521002803)
1077 S0019103521002803 doi: <https://doi.org/10.1016/j.icarus.2021.114616>

1078 Sánchez-Cano, B., Lester, M., Witasse, O., Blelly, P.-L., Indurain, M., Cartacci,
1079 M., ... Noschese, R. (2018). Spatial, seasonal, and solar cycle variations of
1080 the martian total electron content (tec): Is the tec a good tracer for atmo-
1081 spheric cycles? *Journal of Geophysical Research: Planets*, 123(7), 1746-1759.
1082 Retrieved from [https://agupubs.onlinelibrary.wiley.com/doi/abs/](https://agupubs.onlinelibrary.wiley.com/doi/abs/10.1029/2018JE005626)
1083 10.1029/2018JE005626 doi: <https://doi.org/10.1029/2018JE005626>

1084 Sánchez-Cano, B., Morgan, D. D., Witasse, O., Radicella, S. M., Herraiz, M., Orosei,
1085 R., ... Quinsac, G. (2015). Total electron content in the martian atmosphere:
1086 A critical assessment of the mars express marsis data sets. *Journal of Geo-*
1087 *physical Research: Space Physics*, 120(3), 2166-2182. Retrieved from [https://](https://agupubs.onlinelibrary.wiley.com/doi/abs/10.1002/2014JA020630)
1088 agupubs.onlinelibrary.wiley.com/doi/abs/10.1002/2014JA020630 doi:
1089 <https://doi.org/10.1002/2014JA020630>

1090 Sánchez-Cano, B., Narvaez, C., Lester, M., Mendillo, M., Mayyasi, M., Holmstrom,
1091 M., ... Durward, S. (2020). Mars' ionopause: A matter of pressures. *Journal*
1092 *of Geophysical Research: Space Physics*, 125(9), e2020JA028145. Retrieved
1093 from [https://agupubs.onlinelibrary.wiley.com/doi/abs/10.1029/](https://agupubs.onlinelibrary.wiley.com/doi/abs/10.1029/2020JA028145)
1094 2020JA028145 (e2020JA028145 2020JA028145) doi: [https://doi.org/10.1029/](https://doi.org/10.1029/2020JA028145)
1095 2020JA028145

1096 Schneider, N. M., Jain, S. K., Deighan, J., Nasr, C. R., Brain, D. A., Larson, D., ...
1097 Jakosky, B. M. (2018). Global Aurora on Mars During the September 2017
1098 Space Weather Event. *Geophysical Research Letters*, 45(15).

1099 Simms, L. E., Engebretson, M. J., Rodger, C. J., Dimitrakoudis, S., Mann, I. R., &
1100 Chi, P. J. (2021). The combined influence of lower band chorus and ulf waves
1101 on radiation belt electron fluxes at individual l-shells. *Journal of Geophysical*
1102 *Research: Space Physics*, 126(5), e2020JA028755. Retrieved from <https://>

- 1103 agupubs.onlinelibrary.wiley.com/doi/abs/10.1029/2020JA028755
1104 (e2020JA028755 2020JA028755) doi: <https://doi.org/10.1029/2020JA028755>
- 1105 Steckiewicz, M., Garnier, P., André, N., Mitchell, D. L., Andersson, L., Penou,
1106 E., ... Jakosky, B. M. (2017, January). Comparative study of the Mar-
1107 tian suprathermal electron depletions based on Mars Global Surveyor, Mars
1108 Express, and Mars Atmosphere and Volatile Evolution mission observa-
1109 tions. *Journal of Geophysical Research (Space Physics)*, *122*, 857-873. doi:
1110 10.1002/2016JA023205
- 1111 Trotter, G., Samwel, S., Klein, K. L., Dudok De Wit, T., & Miteva, R. (2015). Sta-
1112 tistical Evidence for Contributions of Flares and Coronal Mass Ejections to
1113 Major Solar Energetic Particle Events. *Solar Physics*, *290*(3), 819–839. Re-
1114 trieved from <https://hal-insu.archives-ouvertes.fr/insu-01344581> doi:
1115 10.1007/s11207-014-0628-1
- 1116 Vignes, D., Acuna, M. H., Connerney, J. E. P., Crider, D. H., Reme, H., &
1117 Mazelle, C. (2002). Factors controlling the location of the bow shock at
1118 mars. *Geophysical Research Letters*, *29*(9), 42-1–42-4. Retrieved from
1119 <http://dx.doi.org/10.1029/2001GL014513> doi: 10.1029/2001GL014513
- 1120 Wang, M., Lu, J. Y., Kabin, K., Yuan, H. Z., Ma, X., Liu, Z.-Q., ... Li, G. (2016).
1121 The influence of imf clock angle on the cross section of the tail bow shock.
1122 *Journal of Geophysical Research: Space Physics*, *121*(11), 11,077-11,085.
1123 Retrieved from [https://agupubs.onlinelibrary.wiley.com/doi/abs/](https://agupubs.onlinelibrary.wiley.com/doi/abs/10.1002/2016JA022830)
1124 [10.1002/2016JA022830](https://doi.org/10.1002/2016JA022830) doi: <https://doi.org/10.1002/2016JA022830>
- 1125 Xu, S., Mitchell, D., Liemohn, M., Dong, C., Bougher, S., Fillingim, M., ...
1126 Jakosky, B. (2016, September). Deep nightside photoelectron observations
1127 by MAVEN SWEA: Implications for Martian northern hemispheric magnetic
1128 topology and nightside ionosphere source. *Geophysical Research Letters*, *43*,
1129 8876-8884. doi: 10.1002/2016GL070527
- 1130 Yesuf, H. M., & Ho, L. C. (2019, oct). Dirt-cheap gas scaling relations: Using dust
1131 absorption, metallicity, and galaxy size to predict gas masses for large samples
1132 of galaxies. *The Astrophysical Journal*, *884*(2), 177. Retrieved from [https://](https://doi.org/10.3847/1538-4357/ab4202)
1133 doi.org/10.3847/1538-4357/ab4202 doi: 10.3847/1538-4357/ab4202

